WILEY

Metal chalcogenides for potassium storage

Jingwen Zhou[1,2] | Ye Liu[1] | Shilin Zhang[1] | Tengfei Zhou[1] | Zaiping Guo[1]

[1]Institute for Superconducting and Electronic Materials (ISEM), Australian Institute for Innovative Materials (AIIM), School of Mechanical, Materials, Mechatronics and Biomedical Engineering, University of Wollongong, Wollongong, Australia

[2]Institute of Chemical Materials, China Academy of Engineering Physics, Mianyang, Sichuan, People's Republic of China

Correspondence
Tengfei Zhou and Zaiping Guo, Institute for Superconducting and Electronic Materials (ISEM), Australian Institute for Innovative Materials (AIIM), School of Mechanical, Materials, Mechatronics and Biomedical Engineering, University of Wollongong, Wollongong 2522, Australia.
Email: tengfeiz@uow.edu.au (T. Z) and zguo@uow.edu.au (Z. G)

Funding information
Australian Research Council, Grant/Award Numbers: DE190100504, DP170102406, DP200101862; Chinese Scholarship Council, Grant/Award Number: 201908420279; National Natural Science Foundation of China, Grant/Award Number: 51802357

Abstract

Potassium-based energy storage technologies, especially potassium ion batteries (PIBs), have received great interest over the past decade. A pivotal challenge facing high-performance PIBs is to identify advanced electrode materials that can store the large-radius K^+ ions, as well as to tailor the various thermodynamic parameters. Metal chalcogenides are one of the most promising anode materials, having a high theoretical specific capacity, high in-plane electrical conductivity, and relatively small volume change on charge/discharge. However, the development of metal chalcogenides for PIBs is still in its infancy because of the limited choice of high-performance electrode materials. However, numerous efforts have been made to conquer this challenge. In this article, we overview potassium storage mechanisms, the technical hurdles, and the optimization strategies for metal chalcogenides and highlight how the adjustment of the crystalline structure and choice of the electrolyte affect the electrochemical performance of metal-chalcogenide-based electrode materials. Other potential potassium-based energy storage systems to which metal chalcogenides can be applied are also discussed. Finally, future research directions focusing on metal chalcogenides for potassium storage are proposed.

KEYWORDS

energy storage, metal chalcogenides, modification strategies, nanocomposites, potassium ion batteries

1 | INTRODUCTION

Scientific and technological developments have the potential to affect every part of society. This is particularly the case for lithium-ion batteries (LIBs), which play a role in the daily lives of many people.[1-4] LIBs have made wearable and portable electronics, electric vehicles, and stationary energy storage possible. Further, they allow the prompt exchange of information without the limitations (such as blackouts) inherent to distributed electricity supply systems (ie, national power grids).[5-8] From the perspective of environmental protection, LIBs enable the exploitation of intermittent clean, renewable energy sources such as solar, wind, tide, and terrestrial heat, thus allowing the use of fossil fuels to be reduced, reducing environmental contamination, and restricting pollution and waste production to controlled regions or levels.[9-11] However, the uneven global distribution of lithium and reserve shortages (20 ppm) have resulted in large increases in market price in the past decade, which

---

Jingwen Zhou and Ye Liu contributed equally to this work.

has prevented LIBs from being used in large-scale industries. Thus, sodium and potassium, alkali metal counterparts of lithium, which are present in much higher abundance (23 000 ppm for Na, 17 000 ppm for K) than Li, are popular targets for the development of new rechargeable battery technologies, including sodium-ion batteries (SIBs) and potassium-ion batteries (PIBs), that share a similar "rocking-chair" mechanism with LIBs.[12-14]

In contrast to the standard redox potential of Na+/Na (−2.71 V vs the standard hydrogen electrode [SHE]), that of K+/K (−2.93 V vs SHE) is much lower and even comparable to the redox potential of Li+/Li (−3.04 V vs SHE), indicating that KIBs could achieve a higher working voltage than SIBs and LIBs. However, K has a larger atomic radius (1.38 Å) than Li (0.68 Å) and Na (0.97 Å) atoms but has the smallest solvated ion radius of these three

monovalent alkali metals (3.6 Å for K+, 4.8 Å for Li+, and 4.6 Å for Na+) in propylene carbonate (PC) solvent because of the weaker Lewis acidity of K+.[13,15-19] This is a useful feature of K+-based electrolytes, resulting in high ionic conductivity and fast diffusion kinetics. In addition, some computational simulations have even revealed that the diffusion coefficient of K+ is nearly four times as much as that of Li+.[20-22] As a consequence, graphite, which has been successfully used as the anode material in LIBs, can also be used in PIBs. The intercalation of K+ into graphite is favorable and highly reversible, which is a strong contrast to the inactive electrochemistry of SIBs.[23-25] Based on the above advantages, the replacement of Li+ with K+ for the construction of high-performance K-based energy storage systems with enhanced rate capability, high-mass-loading electrodes, and, thus, higher energy densities is highly promising.[13,26] The schematic
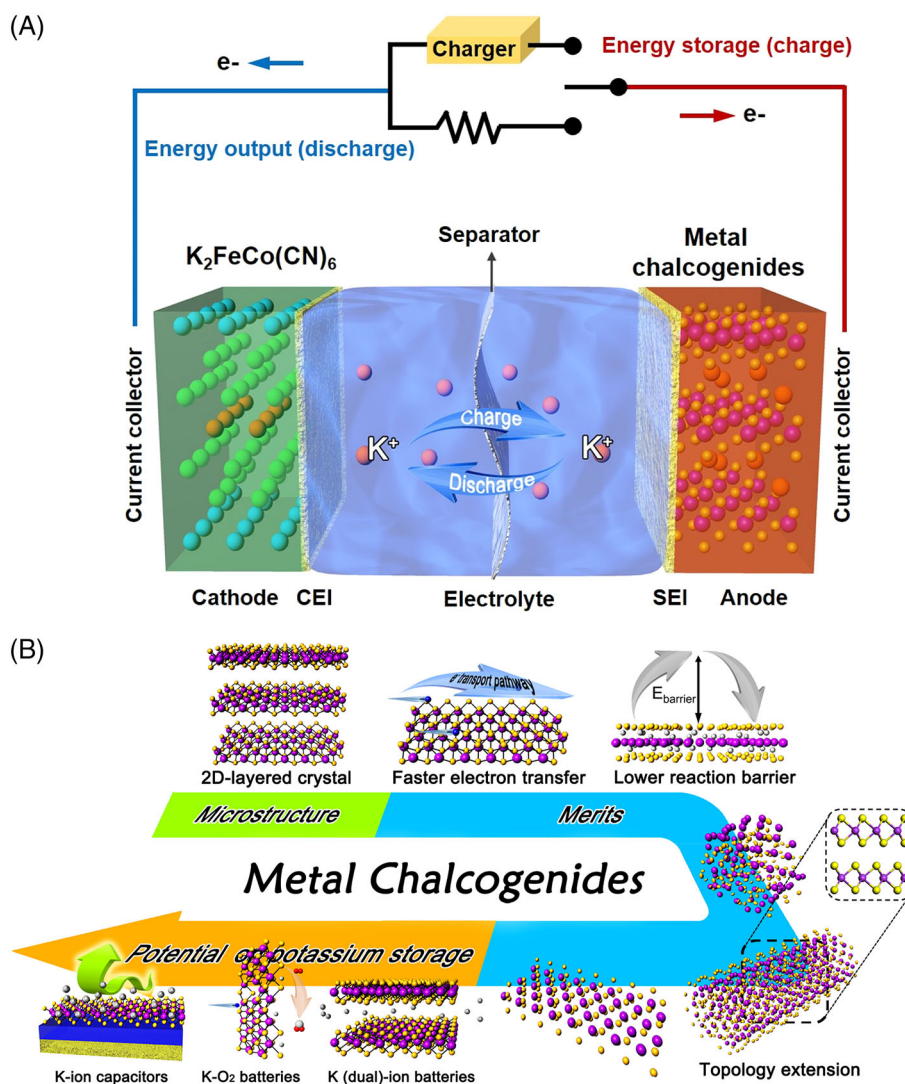

FIGURE 1 A, Schematic depicting the configuration and working principle of a "rocking-chair" potassium-ion battery. B, A general illustration of the microstructure, merits, and potential applications in the field of potassium storage for metal chalcogenides

illustration presented in Figure 1A depicts the general configuration and working principle of "rocking-chair" PIBs.

The first step toward achieving high-performance K^+-based energy storage technologies is to exploit host materials that have superior potassium storage capability and sufficient structural stability to withstand the repeated K^+-ion insertion and extraction processes.[15,16,27] For PIBs, the most representative K^+-based rechargeable energy storage system, the aforementioned target indicates that developing efficient anode materials with the favorable features of high specific capacities, excellent cycling stabilities, and fast diffusion/reaction kinetics is urgently required to advance the progress of current PIBs toward practical applications.[28-30] Inspired by the existing pioneering work involving graphite, tremendous efforts have been devoted to this area of research. To date, several categories of materials are verified to be effective for potassium storage in terms of anodes, including carbon nanophases[29,31-44] (eg, hard carbon, graphite, and heteroatom-doped carbon), alloy-type (semi-)metals[15,16,45-48] (eg, Sn, Bi, Sb, and P), metal oxides[49-52] (eg, Nb_2O_5, SnO_2, Fe_xO, and Sb_2MoO_6)/sulfides[53-57] (eg, MoS_2, VS_2, SnS_2, and Sb_2S_3) and phosphides[58-63] (eg, FeP, CoP, Sn_4P_3, and GeP_5), sylvite compounds[64-70] (eg, $KVPO_4F$, $K_2V_3O_8$, $KTi_2(PO_4)_3$, and $K_xMn_yO_z$), metal-organic composites[71,72] (eg, $Co_3[Co(CN)_6]_2$ and $K_{1.81}Ni[Fe(CN)_6]_{0.97} \cdot 0.086H_2O$), and pure organic polymers[73-79] (eg, boronic ester, fluorinated covalent triazine, perylene-tetracarboxylate, perylenetetracarboxylic diimide, azobenzene-4,4'-dicarboxylic acid potassium, 2,2'-azobis[2-methylpropionitrile], and poly[pyrene-co-benzothiadiazole]). However, most carbon materials barely deliver reversible capacities exceeding 300 mAh g^{-1} despite their excellent electrochemical cyclability. Alloying-type metals suffer huge volume changes and pulverization, leading to unexceptionally rapid capacity decay within 200 cycles. Sylvite compounds together with metal-organic composites reveal more difficulties to be addressed, like tedious preparation, limited capacity, instability, complicated K^+-ion insertion/extraction reactions, and low reliability. Organic polymers usually suffer from low initial Coulombic efficiencies (CEs), limited reversible capacities, and poor rate capabilities due to the severe side reactions between radicals and K^+ ions, inadequate active sites, and low electric/ionic conductivity. Of the examples listed above, metal chalcogenides have received numerous insights from researchers in recent years on account of their large theoretical specific capacity, relatively small volume changes, and higher electrical conductivity compared to oxides and phosphides.[53,80] Most metal chalcogenides possess a two-dimensional (2D) layered structure and have low reaction energy barriers for the storage of alkali metal ions. Because of the easy topological extension, numerous techniques can be utilized to prepare different morphologies of metal chalcogenides having the same crystal structure, thus increasing the possible applications of this material.[14,81] In fact, metal chalcogenides are not limited to K^+-ion battery applications; these materials are "shining stars," having possible applications in K dual-ion batteries, $K-O_2$ batteries, K^+-ion capacitors, and other energy storage and conversion fields, as shown in Figure 1B.[82-86] In PIBs, depending on the different K^+-ion alloying ability of the metal atoms (inactive or active), metal chalcogenides can be divided into two categories: conversion type and conversion/alloying-coupling type. The latter type usually reveals a larger specific capacity because of the contribution to the capacity of the alloying reactions between metal atoms and K^+ ions.

Even though faster K^+-ion reaction kinetics are incorporated into metal-chalcogenide-based PIB anodes, there still remain challenges, unfortunately, including the dissolution and shuttle effect of discharge products (polychalcogenides such as K_xS_y and K_xSe_y), poor ion diffusion in the bulk, and structural instability originating from conversion reactions and agglomeration, which can even result in inactivation caused by volume expansion. Therefore, current metal chalcogenide anodes are still immature and do not deliver satisfactory long-term cycling stability in terms of potassium storage, especially at high rates.[55,80,81] However, an encouraging feature is that, because of the similarity of the energy storage mechanism in metal chalcogenides to that in alkali metal ion batteries, existing modification strategies accumulated for LIBs and SIBs can be potentially transplanted to improve the performance of PIBs.[4,87,88] There are four main approaches to enhance the ionic and electrical conductivity, buffer or accommodate the volume changes, increase the structural integrity and stability, and boost the reaction kinetics of metal chalcogenides (Figure 2): limitation of discharge depth, nanostructure engineering, confinement by carbon nanophases, or ternary alloying. The majority of these modification methods described above have already been verified to be effective for potassium-based energy storage according to the results reported previously.[53,81,89-95] Furthermore, the interface between the anode and electrolyte in PIBs has drawn recent attention and is another non-negligible factor for stabilizing these energy-storage systems. In particular, the category and component of electrolyte are of great significance to determine whether a thin, homogeneous, and stable solid electrolyte interphase (SEI) with high ionic conductivity is formed on the surface of metal chalcogenide-based anode materials, which results in different structural and surface properties.[62,96,97] The SEI is one of the most crucial features that affect the stable long-term cycling performance of batteries. Simultaneously, optimization to achieve the best match of anode material and electrolyte
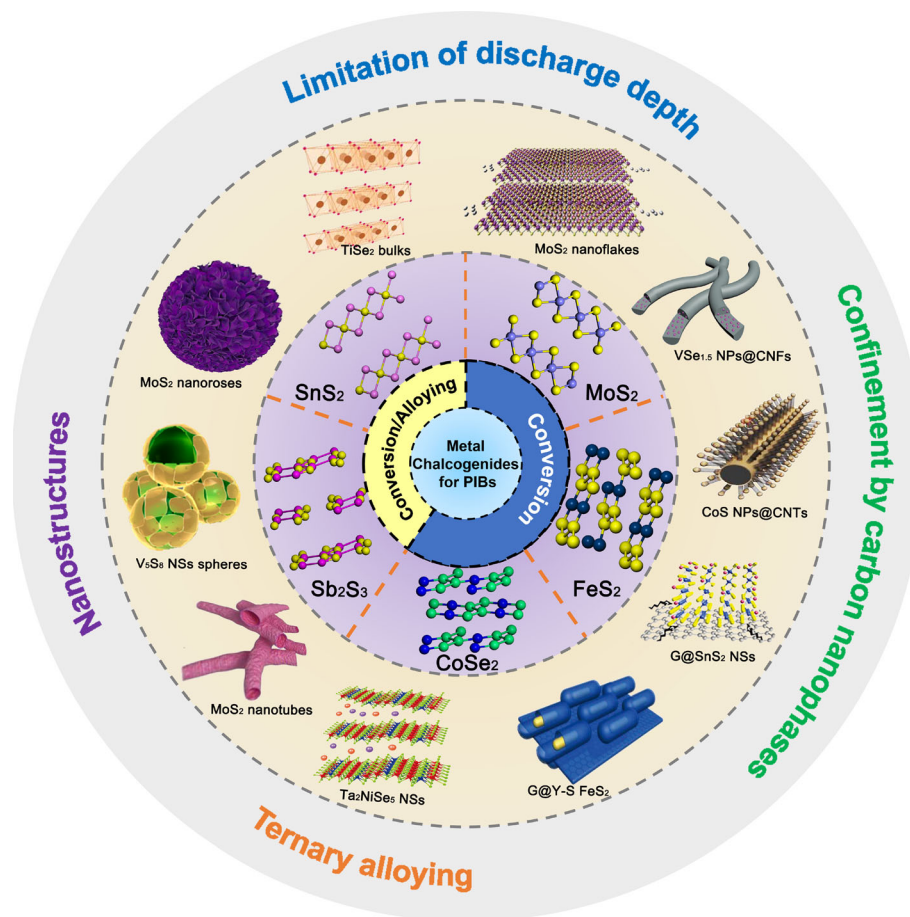
FIGURE 2 Illustration of the classification and dominant modification strategies that have been reported for metal chalcogenides-based PIB anodes. Some of the inset pictures are reproduced with permission from Wiley-VCH, American Chemical Society, The Royal Society of Chemistry and Elsevier[53,81,89-95]

is also crucial to minimize parasitic reactions and achieve a wide voltage window and large capacity, thus further improving the energy density and working life of PIBs. On the other hand, improving the potassium storage capability of metal-chalcogenide-based materials will not only aid the development of PIBs as high-performance power storage devices but will also facilitate the development of other novel rechargeable systems on the basis of K^+-ion storage mechanism (such as K-S/Se batteries, K dual-ion batteries, K^+-ion battery capacitors, and K-O_2 batteries) for advanced and practical energy storage applications.[98-101]

In this research progress report, key technical advances and dominated hurdles facing current metal chalcogenide-based PIBs are discussed, with emphasis on how the structure, components, and properties of anode materials synthesized using different strategies affect the electrochemical performance of the assembled PIBs. Meanwhile, the main modification strategies are summarized by exemplifying several previous metal-chalcogenide-based nanostructures and nanocomposites which are

particularly designed or prepared. The underlying reasons for the effectiveness of these modifications are proposed as well based on our considerations and reported experimental results. In addition, other representative K^+-based novel energy storage systems using metal-chalcogenide-based materials are given to illustrate their great potential for potassium storage further. Finally, we share our insights into the present challenges and possible future research directions, hoping to provide some inspirations for the design and fabrication of high-performance metal chalcogenide-based anode materials for PIBs and other advanced K^+-ion energy storage systems.

2 | METAL CHALCOGENIDE ANODES FOR PIBs

For metal chalcogenides utilized for PIB anodes, they can be mainly classified into two categories according to their different potassium insertion (potassiation) processes:

TABLE 1 Comparison of the synthesis, reaction mechanisms, test methods, electrolytes, ICEs, ISCs for long-term cycling and potassium storage capability for several typical metal-chalcogenide-based materials used as anode materials for PIBs

Anode	Synthesis	Discharge products	Charge products	Test methods	Electrolyte	ICE (%)	ISC (mAh g$^-$)	Potassium storage capability
TiSe$_2$ powders[89]	Commercial products	K$_{0.8}$TiSe$_2$	K$_{0.24}$TiSe$_2$	In situ XRD	0.8 M KPF$_6$ in EC/DEC	90	65	59.7 mAh g^{-1} after 80 cycles at 0.056 A g^{-1}; 52.2 mAh g^{-1} after 300 cycles at 0.15 A g^{-1}
TiS$_2$[106]	Commercial products	K$_{0.11}$TiS$_2$+ K$_{0.56}$TiS$_2$	TiS$_2$	Ex situ XRD + HRTEM	1.0 M KPF$_6$ in DME	77.7	80	91 mAh g^{-1} after 100 cycles at 0.48 A g^{-1}; 63 mAh g^{-1} at 600th cycle at 4.8 A g^{-1}
K$_{0.25}$TiS$_2$[107]	Prepotassiation from TiS$_2$	5^K (K$_{0.25}$TiS$_2$)	3^K (K$_{0.25}$TiS$_2$)	Ex situ XRD + HRTEM	0.8 M KPF$_6$ in EC/DEC	104.2 (pre-potassiation)	151.1	151.1 mAh g^{-1} after 100 cycles at 0.024 A g^{-1}
NCNTs@CoSe$_2$[20]	CVD hydrothermal growth	Co + K$_2$Se		DFT calculation	0.8 M KPF$_6$ in EC/DEC	69.3	196	253 mAh g^{-1} after 100 cycles at 0.2 A g^{-1}; 173 mAh g^{-1} after 600 cycles at 2.0 A g^{-1}
MoS$_2$/N-C[90]	Solvothermal growth + annealing	Mo + K$_x$S$_y$		Ex situ Raman + HRTEM			220	248 mAh g^{-1} after 100 cycles at 0.1 A g^{-1}; 151 mAh g^{-1} after 1000 cycles at 0.5 A g^{-1}
V$_5$S$_8$/C nanosheets[81]	Solvothermal growth + annealing	KV$_5$S$_8$ + K$_2$S$_3$ + V	V$_5$S$_8$	Ex situ XRD	1 M KFSI in EC/PC	64	240	501 mAh g^{-1} after 100 cycles at 0.05 A g^{-1}; 190 mAh g^{-1} after 1000 cycles at 2 A g^{-1}
VS$_2$ nanosheets[103]	Solvothermal growth				0.5 M KPF$_6$ in EC/EDC	70	290	410 mAh g^{-1} after 60 cycles at 0.1 A g^{-1}; 360 mAh g^{-1} after 100 cycles at 0.5 A g^{-1}
MoSe$_2$/N-C[96]	Hydrothermal growth	MoO$_x$ + K$_5$Se$_3$+ K$_2$Se$_2$ + K$_2$Se	Mo$_{15}$Se$_{19}$ + MoSe$_2$ + Se	Ex situ XRD and Raman + HRTEM	1 M KFSI in EMC	79.9	278.3	258.2 mAh g^{-1} after 300 cycles at 0.1 A g^{-1}
MoS$_2$/rGO[53]	Hydrothermal growth	K$_2$S + Mo	MoS$_2$	Ex situ XRD and Raman	1 M KPF$_6$ in EC/DEC/PC	72.2	363.2	416.7 mAh g^{-1} after 200 cycles at 0.1 A g^{-1}; 424.6 mAh g^{-1} after 1000 cycles at 0.5 A g^{-1}
Sb$_2$S$_3$/C nanosheets[55]	Solution-triggered exfoliation	K$_3$Sb + K$_2$S$_3$		In situ synchrotron XRD	1 M KSiF$_6$ in EC/PC	39	~505	~500 mAh g^{-1} after 50 cycles at 0.05 A g^{-1}
Sb$_2$Se$_3$@C microtubes[105]	Mixed solution + calcination sulfuration	K$_3$Sb + K$_2$Se$_3$	Sb$_2$Se$_3$	In situ Raman	0.8 M KPF$_6$ in EC/PC	50	~250	312.8 mAh g^{-1} after 40 cycles at 0.1 A g^{-1}; 191.4 mAh g^{-1} after 400 cycles at 0.5 A g^{-1}
rGO/SnS$_2$[93]	Mixed solution	KSn + K$_4$Sn$_{23}$ + K$_2$S + K$_2$S$_5$	SnS + K$_2$S$_5$	Ex situ XRD + HRTEM	0.8 M KPF$_6$ in EC/DEC	51.2	280.8	387 mAh g^{-1} after 100 cycles at 0.05 A g^{-1}; 205 mAh g^{-1} after 300 cycles at 1 A g^{-1}
VSe$_{1.5}$@CNFs[95]	Electrospinning + calcination selenylation				1 M KFSI in DME	55	190	313 mAh g^{-1} after 40 cycles at 0.1 A g^{-1}; 177 mAh g^{-1} after 100 cycles at 1 A g^{-1}
FeS$_2$@CNFs[80]	Electrospinning + calcination sulfuration				1 M KCF$_3$SO$_3$ in EC/DMC	62.4	193.5	obvious decay at 0.2 A g^{-1}; 120 mAh g^{-1} after 680 cycles at 1 A g^{-1}

(Continues)

TABLE 1 (Continued)

| Anode	Synthesis	Discharge products	Charge products	Test methods	Electrolyte	ICE (%)	ISC (mAh g⁻)	Potassium storage capability
WS_2[108]	Commercial products	$K_{0.62}WS_2$	WS_2	In situ XRD + HRTEM	5.0 M KTFSI in TEGDME	56.6	39	56.6 mAh g^{-1} after 100 cycles at 0.005 A g^{-1}; ~43 mAh g^{-1} after 500 cycles at 0.2 A g^{-1}
WS_2[109]	Commercial products			Ex situ XRD and Raman	1.0 M KPF$_6$ in EC/PC	56.0	52	103 mAh g^{-1} after 100 cycles at 0.1 A g^{-1}; 48.2 mAh g^{-1} after 400 cycles at 0.5 A g^{-1}
CoS_x/NCNT-CNF[94]	Electrospinning + in situ CVD	Co + K_2S	CoS	Ex situ XRD	0.8 M KPF$_6$ in EC/DEC	57.6	~180	125 mAh g^{-1} after 600 cycles at 3.2 A g^{-1}; obvious decay within initial 100 cycles
CoS quantum dots[102]	Solvothermal growth + annealing				0.6 M KPF$_6$ in EC/DEC	64.4	675	310.8 mA h g^{-1} after 100 cycle at 0.5 A g^{-1}
Co_9S_8 dual shells[110]	Solvothermal growth + annealing	$K_xCo_9S_8$ + Co + K_2S	Co_9S_8		0.6 M KPF$_6$ in EC/DEC	40.9	222.7	320.5 mAh g^{-1} after 200 cycles at 0.1 A g^{-1}; 163.9 mAh g^{-1} after 1000 cycles at 1.0 A g^{-1}
NiS_x@C nanosheets[111]	Mixed solution + calcination sulfuration				0.5 M KPF$_6$ in EC/PC	34	~310	300 mAh g^{-1} after 300 cycles at 0.1 A g^{-1}; 128 mAh g^{-1} after 8000 cycles at 0.5 A g^{-1}
rGO/FeS_2@C[92]	Mixed solution + calcination sulfuration	Fe + K_2S	K_xFeS_2	Ex situ XRD + HRTEM	1 M KPF$_6$ in EC/PC	36	295	308 mAh g^{-1} after 100 cycles at 0.3 A g^{-1}; 100 mAh g^{-1} after 1500 cycles at 5 A g^{-1}
ZnS/C@rGO[56]	Solvothermal growth + annealing	K_2S + KZn_x	ZnS	Ex situ XPS + TEM	1 M KPF$_6$ in EC/DEC	63.6	~620	obvious decay within 10 cycles; 330 mAh g^{-1} after 100 cycles at 0.05 A g^{-1}; 208 mAh g^{-1} after 300 cycles at 0.5 A g^{-1}
MoSSe alloys[112]	Vacuum calcination				1 M KFSI in EC/DEC	77.9	310	526.8 mAh g^{-1} after 100 cycles at 0.1 A g^{-1}; 220.5 mAh g^{-1} after 1000 cycles at 2 A g^{-1}
$SnSb_2Te_4$/G[97]	Ball-milling				1 M KFSI in DMC	77.9	383.8	350 mAh g^{-1} after 200 cycles at 0.5 A g^{-1}
Ta_2NiSe_5 flakes[91]	Ion-assisted exfoliation	Ni + Ta + K_2Se	Ta_2NiSe_5	Ex situ Raman and XRD + HRTEM	0.8 M KPF$_6$ in EC/DEC + 10% FEC	70	142.5	315 mAh g^{-1} after 50 cycles at 0.05 A g^{-1}; 116 mAh g^{-1} after 1100 cycles at 0.5 A g^{-1}
ReS_2/NCNFs[113]	Electrospinning + solvothermal growth + annealing				0.8 M KTFSI in DME	67.3	364	253 mAh g^{-1} after 100 cycles at 0.05 A g^{-1};
$ReSe_2$@G@CNFs[114]	Electrospinning annealing	K_xReSe_2 + K_2Se + Re	$ReSe_2$		3.0 M KFSI in DME	62.0	237.1	230 mAh g^{-1} after 200 cycles at 0.2 A g^{-1}; 212 mAh g^{-1} after 150 cycles at 0.5 A g^{-1}
$Bi_{1.11}Sb_{0.89}S_3$ nanotubes[115]	Coprecipitation	$K_3(Bi,Sb)$ + K_2S_4	Bi,Sb + S	In operando XRD	3 M KFSI in DME	59.8	452.6	600 mAh g^{-1} after 10 cycles at 0.1 A g^{-1}; 353 mAh g^{-1} after 1000 cycles at 0.5 A g^{-1}

Abbreviations: CVD, chemical vapor deposition; DEC, diethylcarbonate; DFT, density functional theory; DME, dimethoxyethane; ICE, initial Coulombic efficiency; ISC, initial specific capacity; KTFSI, potassium bis(trifluoromethane)sulfonimide; PC, propylene carbonate; PIB, potassium ion battery; TEM, transmission electron microscopy; XRD, X-ray diffractometry.

conversion type and conversion/alloying-coupling type. The former consists of electrochemically inactive metal atoms (such as Co, Fe, Ni, Mo, and V)[53,102,103] and chalcogens, whereas the latter is comprised of active metal atoms with the ability to store potassium through alloying reactions with metals (such as Sn, Sb, and Ge)[93,104,105] and chalcogens. In common cases, conversion/alloying-coupling type metal chalcogenides deliver higher specific capacities but suffer from greater volume expansion than their individual conversion-type counterparts. How to keep a good balance between the capacity and structural integrity underlies the road for metal chalcogenides toward ideal potassium host materials. Although the cycling stability of metal chalcogenides does not currently exceed that of traditional intercalation-type materials, such as carbon and sylvite compounds, it is still attractive enough to merit the exploration of metal chalcogenides with specially designed microstructures or chemical components/states as anode materials for PIBs, due to their remarkably higher theoretical specific capacities. Hence, in the following sections, we illustrate recently developed metal-chalcogenide-based composites anode materials for PIBs, focusing on the aspects of potassium storage mechanisms, design, synthesis methods, measurements, modification strategies, and corresponding performances. To provide a more comprehensive and systematic report, several representative examples are summarized in Table 1 before discussing the details.[20,53,55,56,80,89-97,102,103,105-115]

2.1 | Potassium storage mechanism of metal chalcogenides

As mentioned above, metal chalcogenides for PIBs can be divided into two categories according to the reactivity of the metal components with potassium ions.

(1) *Conversion-type metal chalcogenides*. Representatives of this kind of metal (inactive) chalcogenide are MoS_2, $MoSe_2$, FeS_2, ZnS, $CoSe_{1.5}$, and V_5S_8.[20,90,96,103] The chalcogen component in these compounds is responsible for the vast majority of the capacity, and the inactive metals provide little contribution, except for the part from interfacial storage between metal atoms and chalcogens/potassium polychalcogenides after their reduction to a metallic phase during the potassiation process. Despite their little contribution to the capacity, these metal atoms form a continuously conductive network pinned in the compound, which not only enhances the overall electric conductivity but also serves as a soft substrate to buffer volume changes. The general potassiation/depotassiation reaction mechanism is shown in Equation (1).

$$M_xC_y + yzK^+ + yze^- \rightleftharpoons xM\cdots yK_zC \quad (1)$$
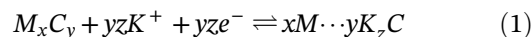
Here, x and y indicate the stoichiometry of the chemical components of metal chalcogenide, and z is the number of combined/extracted potassium ions reacting with the chalcogens ($2 \leq z \leq 8$, z depends on reaction kinetics, which differ remarkably between materials). M and C represent the metal and chalcogen, respectively. During the initial discharge, the metal (inactive) chalcogenides combine with K^+-ions and electrons, becoming transformed into single-phase metal atoms embedded in potassium polychalcogenidess (compounds, $xM...K_zC$). In the first charge process, the $xM...K_zC$ compounds can be oxidized by releasing K^+ ions and electrons to regenerate the metal chalcogen. Of note, on the basis of current experimental results, it is widely recognized that the conversion reactions of metal chalcogenides seem to be not completely reversible in most PIBs. In other words, the phase transformation is partially irreversible, and some new metal chalcogenide phases (with a stoichiometric ratio other than x/y), chalcogens (eg, S and Se) and potassium polychalcogenides (without full depotassiation) are usually formed in association with the conversion of $xM...K_zC$ to M_xC_y.

Assuming that K_zC is the final discharge product, the theoretical specific capacity of conversion-type metal chalcogenides can be calculated using Equation (2).

$$C = \frac{yzF}{3.6r_{(MxCy)}} \quad (2)$$

Here, F is the Faraday constant (96485), and r is the relative molecular mass of the metal (inactive) chalcogenide. The corresponding unit of measurement is milliampere hours per gram (mAh g^{-1}).

(2) *Conversion/alloying-coupling-type metal chalcogenides*. The (active) metal atoms that constitute this kind of metal chalcogenides are commonly metallic elements of groups 14 and 15 with large atomic numbers, such as Ge, Sn, Sb, and Bi, and corresponding metal chalcogenides are represented by Sb_2S_3, SnS_2, and $GeSe$.[55,93,104,105] Both metal and chalcogen components are capable of reversible alloying with K^+, so they can deliver significantly higher capacities but often suffer from more severe volume expansion during the potassiation process. Hence, this category of metal (active) chalcogenides faces several challenges regarding structural instability. The potassiation/depotassiation mechanisms can be specified in Equation (3).

$$M_xC_y + (yz+w)K^+ + (yz+w)e^- \rightleftharpoons M_xK_w\cdots yK_zC \quad (3)$$
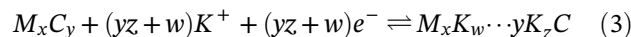
Here, w is the number of combined/extracted potassium ions reacting with the metal. This is also decided by

the reaction kinetics, which is itself affected by the morphology, microstructure, and components of the metal (active) chalcogenides. Similarly, during the initial discharge process, metal-potassium alloy clusters become entangled and potassium polychalcogenides ($M_xK_w...K_zC$) are produced in the form of aggregates after the full potassiation via conversion and alloying reactions. Upon recharging, K^+ ions are extracted from the discharge products, resulting in the reappearance of metal (active) chalcogenides. Currently, it is also considered that only a portion of the metal-potassium alloy/polychalcogenides ($M_xK_w...K_zC$) clusters can return to the original state (M_xC_y) based on current cognition, while metal chalcogenides in other new phases, chalcogens, and potassium polychalcogenides are highly possible to exist during the charging process, which is similar to the situation with their inactive counterparts.

Assuming that M_xK_w and K_zC are the final discharge products, the theoretical specific capacity of conversion/alloying-coupling-type metal chalcogenides can be calculated using Equation (4).

$$C = \frac{(yz + w)F}{3.6R_{(MxCy)}} \quad (4)$$

Here, R is the relative molecular mass of the metal (active) chalcogenides.

The detailed K storage mechanisms of these two kinds of metal chalcogenides are exemplified by several impressive works employing ex situ and in situ X-ray (or synchrotron radiation) diffractometry (XRD), Raman spectroscopy, scanning electron microscopy (SEM), and transmission electron microscopy (TEM) as the main phase characterization techniques. For example, Lu's group investigated the potassiation/depotassiation mechanisms of $MoSe_2$ for the first time by analyzing the ex situ XRD patterns and Raman spectra of the PIB anodes at different states of charge and discharge.[96] After being fully discharged, the $MoSe_2$ anode materials yielded a diffraction pattern in which the characteristic reflections of $MoSe_2$ were hard to be detected. In contrast, reflections corresponding to two potassium polychalcogenide species (K_5Se_3 and K_2Se_2) were observed. More interestingly, in the fully recharged state, elemental Se and $Mo_{15}Se_{19}$ were easily identified, unlike $MoSe_2$, indicating an irreversible part of the recovery from Mo or MoO_x to $MoSe_2$. Because Se still remains in the system, it inevitably participates in K-Se redox reactions obeying analogous K-Se mechanism that are similar to that in Li-S batteries. The Raman spectra also give a proof of the partial reversibility. Furthermore, the detailed phase transformation of $MoSe_2$-Mo/K_xSe-$MoSe_2$/$Mo_{15}Se_{19}$/Se in one cycle was determined by

analyzing XRD patterns obtained at different discharge/charge voltages. It was deduced that the electrochemical potassiation of $MoSe_2$ proceeds in two steps: K^+ intercalation ($MoSe_2 + K^+ + xe^- \rightarrow K_xMoSe_2$, $E > 0.53$ V vs K^+/K) and conversion ($K_xMoSe_2 + (10 - 3x)K^+ + (10 - 3x)$ $e^- \rightarrow 2K_5Se_3 + 3Mo$, $E < 0.53$ V vs K^+/K), and the production of $MoSe_2$, $Mo_{15}Se_{19}$, and Se mainly occurs in the voltage range of 2 to 3 V upon recharging.

Guan's group investigated the potassium storage mechanism of FeS_2.[92] The cyclic voltammetry (CV) and XRD results presented in Figure 3A-C illustrate that when the discharge voltage declines to 1.1 V, the peak intensity of the FeS_2 phase is significantly reduced, while a small peak corresponding to $KFeS_2$ starts to emerge, suggesting the intercalation of K^+ into FeS_2 interlayers to form K_xFeS_2. After discharging the anode to 0.5 V, only a small peak of Fe phase can be recognized in the XRD pattern. When the electrode was totally discharged, no obvious XRD peaks can be found probably due to the low crystallinity or the tiny particle size in discharge products. However, after the electrode was recharged to 2.8 V, peaks corresponding to $KFeS_2$ and K_2S phases were mainly observed, indicating that the final charge product is K_xFeS_2. Interestingly, some of the potassium chalcogenides reveal quite a sluggish reaction kinetics, even losing chemical activity on de-alloying. Moreover, the TEM results further prove that Fe and $KFeS_2$ are embedded in the discharge and charge products, respectively, which is consistent with the XRD analysis. As a result, the group concluded that the initial phase transformation between FeS_2 and K_xFeS_2 is an irreversible potassiation reaction, despite the reversibility of the deeper intercalation and conversion stages, as exhibited in Figure 3D.

Guo's group pioneered the exploration of Sb_2S_3 as an anode material for PIBs.[55] They employed in operando synchrotron XRD ($\lambda = 0.6888$ Å) to understand the phase evolution of Sb_2S_3 during discharge/charge, as shown in Figure 3E. The shift to smaller diffraction angles associated with Sb_2S_3 above 0.7 V is evidence for the intercalation of K^+, which expands the interlayer distance of Sb_2S_3 (Figure 3F). When Sb_2S_3 was discharged from 0.7 to 0.5 V, diffraction peaks assigned to Sb emerged, indicating the presence of conversion reactions. When the voltage reached 0.1 V, peaks ascribed to K_2S_6, K_2S_3, and K_3Sb were generated, but they were weak and broad because of the nanocrystallinity. Encouragingly, ex situ selected area electron diffraction (SAED) investigation confirmed the presence of K_2S_6 and Sb as intermediate products on the basis of their polycrystalline diffraction rings. Thus, the potassiation mechanism for Sb_2S_3 can be summarized by Equations (5)-(7).
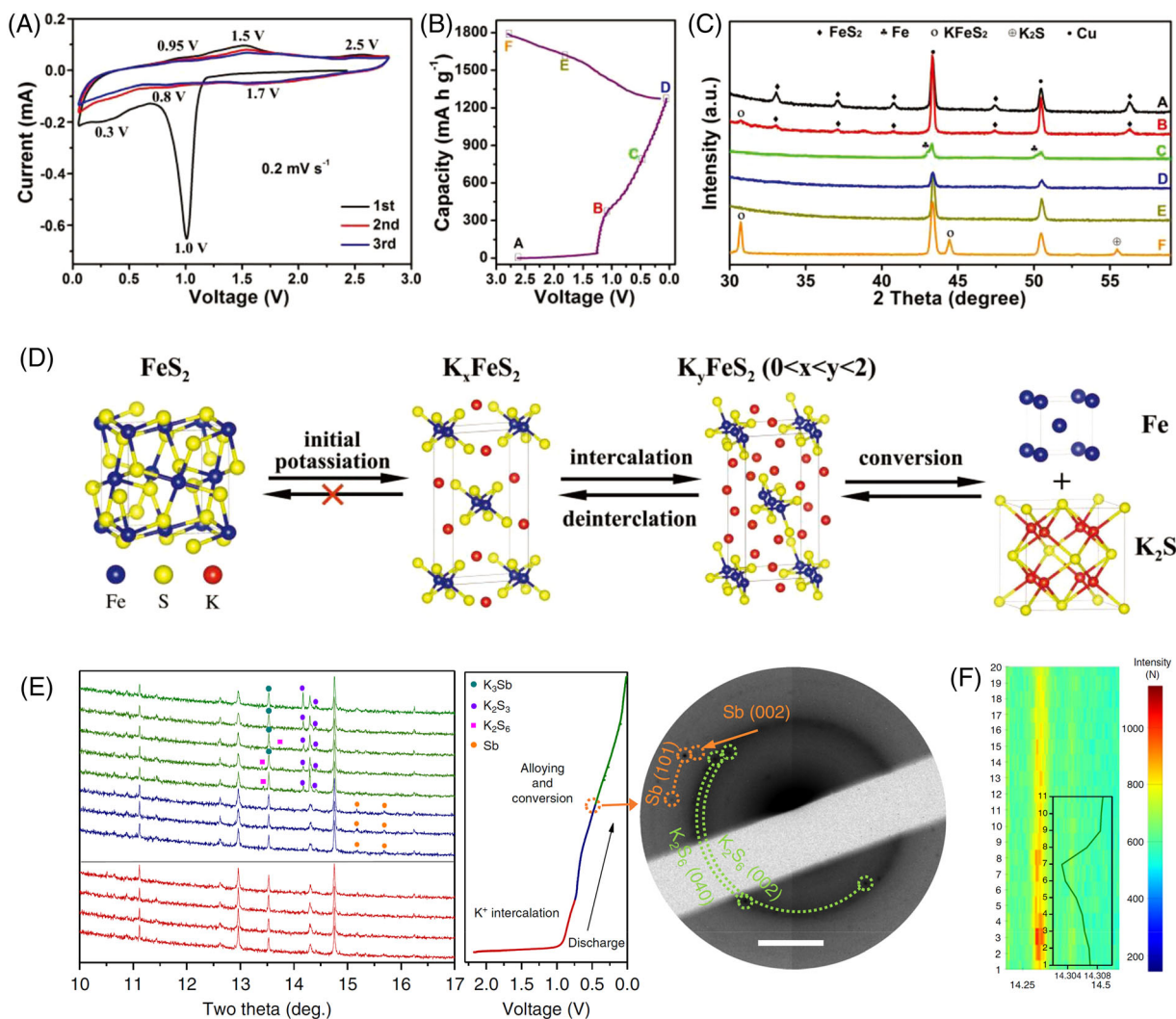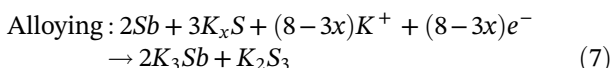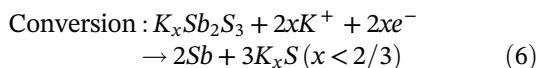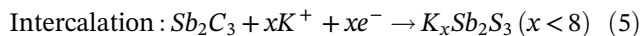
FIGURE 3 A, Cyclic voltammetry (CV) curves; B, initial discharge/charge curves and C, ex situ X-ray diffractometry (XRD) patterns at various states of pure FeS$_2$ anode. D, Schematic illustration for its potassium storage reaction mechanism. Reproduced with permission from Reference 92 Copyright 2018, Wiley-VCH. E, In situ synchrotron XRD patterns of Sb$_2$S$_3$ upon K insertion (left) and ex situ selected area electron diffraction (SAED) pattern (right) at 0.5 V. F, Image plots of the (212) reflection and corresponding fitted peak. Reproduced with permission from Reference 55 Copyright 2018, Nature Publication Group

$$\text{Intercalation}: Sb_2C_3 + xK^+ + xe^- \rightarrow K_xSb_2S_3 \ (x<8) \quad (5)$$

$$\begin{aligned}\text{Conversion}: K_xSb_2S_3 + 2xK^+ + 2xe^- \\ \rightarrow 2Sb + 3K_xS \ (x<2/3)\end{aligned} \quad (6)$$

$$\begin{aligned}\text{Alloying}: 2Sb + 3K_xS + (8-3x)K^+ + (8-3x)e^- \\ \rightarrow 2K_3Sb + K_2S_3\end{aligned} \quad (7)$$

Whereas the phase evolution during charging was not involved in the literature, aside from the confirmation of the presence of undecomposed K$_3$Sb and K$_2$S$_3$ in the recharged products. In addition, Guo et al proposed that the continuous pulverization of Sb$_2$S$_3$ particles caused by the huge volume change (ca. 300%) during cycling is responsible for the rapid decay in capacity. In addition,

Xia's group investigated the potassiation/depotassiation behavior of SnS$_2$ using ex situ XRD, TEM, and SAED measurements.[93] According to the XRD results, the conversion reaction of SnS$_2$ begins above 1.0 V, as shown by the presence of diffraction peaks corresponding to SnS, K$_2$S$_5$, and K$_2$S. Subsequently, further conversion and alloying reactions occur, and the dominant capacity contribution occurs between 0.01 and 0.5 V. The final discharge products were determined to be KSn and K$_2$S (primary) and α-Sn and K$_4$Sn$_{23}$ (minor). However, even though the electrode was recharged to 2.0 V, only SnS coupled with K$_2$S (instead of SnS$_2$) could be found. These findings were confirmed by the TEM analysis of the fully discharged/charged electrodes.

These aforementioned works sufficiently reveal that, for metal-chalcogenide-based PIB anodes, the potassiation

and depotassiation depth intimately relies on their morphology, microstructure, components, and interfacial bonding, and phase transformation is very likely to be incompletely reversible. In addition, the decomposition kinetics for potassium polychalcogenides is commonly not fast enough, resulting in remnant K_zC in the fully recharged electrodes.

2.2 | Challenges facing metal chalcogenides

Even though, a few metal chalcogenides have been proven to be electrochemically active when employed for potassium storage, it does not mean that there are no scientific issues and technical hurdles before discussing the feasibility of metal chalcogenides for practical PIBs and other K-based energy storage systems.[13,15,116] These challenges facing current metal chalcogenide anodes can be mainly concluded as the following aspects:

1. In most metal chalcogenides (mainly sulfides/selenides), potassium polychalcogenides are generated during the deep potassiation process (discharge voltage cutoff: 0.005 V), which may result in detrimental shuttle effects similar to those observed in Li-S batteries. The parasitic reactions between highly reductive potassium metal (in PIB half-cells or other systems with potassium metal anodes) and potassium polychalcogenides produce a K_2C film on the metal anode surface, which blocks the channels for K^+-ion diffusion, thus dramatically decreasing the capacity within the initial cycles and even shutting down the battery suddenly. This is also a potential disadvantage for PIB full cells, which do not employ potassium metal as the anode, because cathode materials commonly exhibit a certain degree of reducibility. Simultaneously, affected by the above unfavorable factors, the evaluation of the potassium storage capability via half-cell methods imposes further burdens on matching the capacity of anodes and cathodes for full-cell PIBs.

2. The huge volume change and incompletely reversible phase transformation during discharge/charge cycles lead to serious structural instability in metal chalcogenides. Obviously, On the one hand, incompletely reversible redox reactions result in the loss of some active components during the depotassiation processes, and, hence, the reversible specific capacity is gradually downward in the following cycles. On the other hand, the tremendous volume change is the chief culprit of the pulverization of active materials and even the exfoliation from the current collectors.

This results in the accumulation of electrochemically inert components in the electrode. This is the dominant reason why most present metal chalcogenides demonstrate unsatisfactory cycling stability.

3. The intrinsically limited electric and ionic conductivities hamper both electron transport and K^+-ion diffusion in bulk metal chalcogenides, leading to a sluggish reaction kinetics, as well as the low utilization efficiency of active sites. As a result, large electrochemical polarization and remarkable capacity decay are easily observed in the measurements at high rates.

4. The instability of SEI is another difficulty that needs to be addressed urgently for metal chalcogenides. The significant volume expansion and shrinkage during cycling destroys the generated SEI film in the initial stages of use, and the newly exposed metal chalcogenides react with K^+ ions to form a new SEI coating. The repeated generation and destruction of the SEI results in the excess consumption of K^+ ions, thereby lowering the CE. Simultaneously, due to the high activity of potassium salts, traditional electrolyte components for LIBs and SIBs seem to be not so much effective for PIBs. Although a dozen combinations of potassium salts and solvents have been attempted as electrolytes for PIBs, it still remains challenging to construct an ideal SEI film having high ionic conductivity, sufficient mechanical ductility and strength, and satisfactory chemical stability, especially for certain categories of anode materials.

2.3 | Optimization strategies for metal chalcogenides

On the way to pursuing suitable metal chalcogenides for PIBs with excellent long-term cycling stability at high rates, numerous efforts have been devoted to materials modification. Benefitting from the long history of research into LIBs, quite a few metal-chalcogenide-based nanostructures and nanocomposites having enhanced potassium storage capabilities have been designed and synthesized. For convenient comparison, the electrochemical performance of typically modified metal chalcogenides for PIBs has been concluded in Figure 4A.[20,53,55,56,80,81,89-97,111,112,115] As shown, there is still large room for improvement, especially concerning the large capacity, low discharge voltage, and long-term cycling stability. Currently, there are four main modification strategies: limitation of discharge depth, nanostructure engineering, confinement by carbon nanophases, and ternary alloying. In the following section, we discuss the advantageous and disadvantageous features of each strategy are exemplified using recent impressive works.

Besides, we also propose a road map for the future development of metal chalcogenides before the discussing. As shown in Figure 4B, we define two conceptual promotion strategies: "inner design" and "outer design." Inner design involves the selection of the most favorable electrolyte components and cycling conditions for certain kinds of metal chalcogenides, thus obtaining the most adaptable couples, whereas outer design involves changing the material's properties or constructing/manipulating the SEI, thus overcoming the intrinsic weakness of metal chalcogenides by artificial solutions. These two strategies will have significantly positive effects on the electrochemical performance of PIB anodes.[117,118] Meanwhile, computational simulations[119,120] and in situ characterization[121,122] will help us understand the underlying potassiation/depotassiation mechanisms and, thus, develop metal chalcogenides for high-performance PIB anodes that are suitable for industrial production.[123] Of course, better performance implies the presence of more compatible interfaces (anode/SEI and SEI/electrolyte, of which the structures, components, and mechanisms are unclear at the present stage of research) in PIBs, and investigation in this area will in turn, accelerate the advance of system design.[124,125]
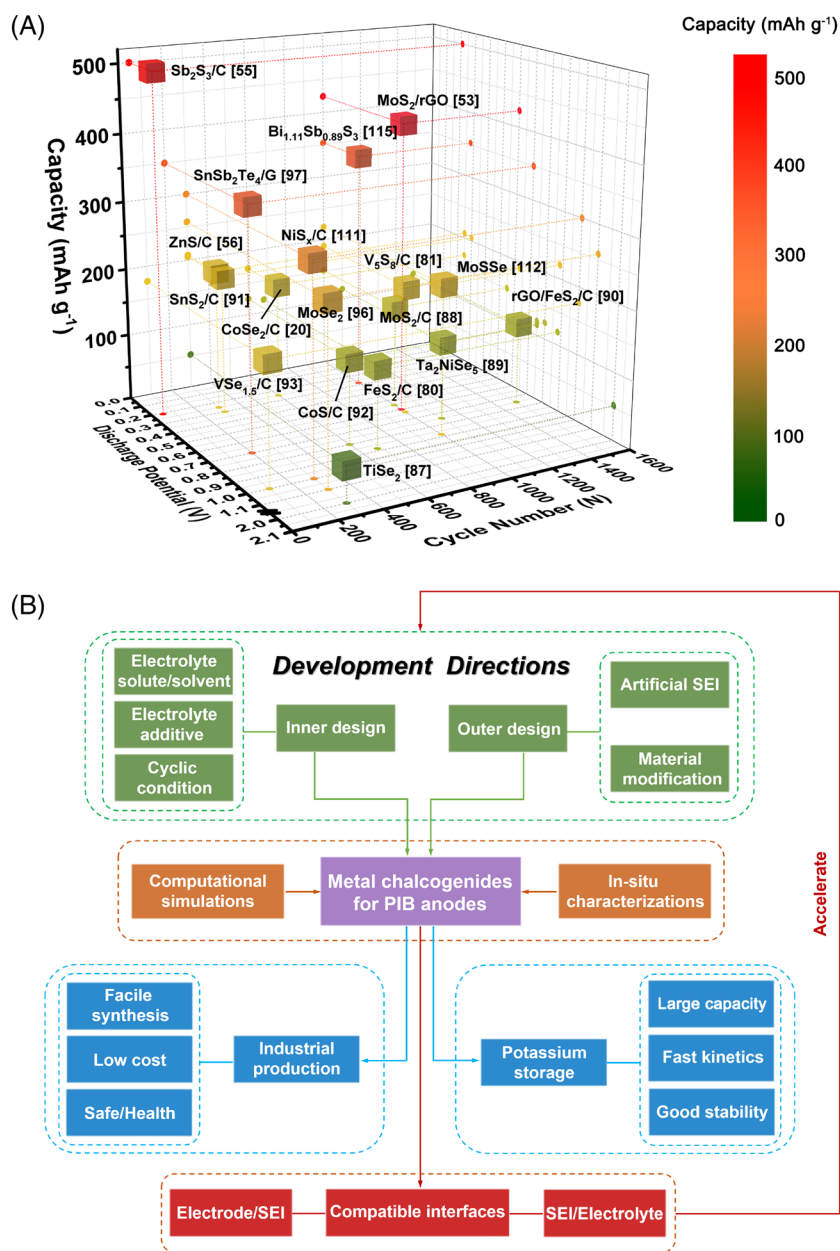

FIGURE 4　A, Summary of electrochemical performances of representative metal chalcogenides-based materials for potassium ion battery (PIB) anodes reported to date.[20,53,55,56,80,81,89-97,111,112,115] B, Future research focuses on metal chalcogenides for PIBs

2.3.1 | Limitation of discharge depth

For most conversion-type metal (inactive) chalcogenides, there is usually an intercalation reaction before the conversion reaction during discharge. The corresponding intercalation mechanism is similar to the mode of intercalating K^+ ions into graphite.[108,126] Therefore, relatively small volume expansion occurs at this stage of potassiation and the structural integrity is well maintained. Because there are no conversion reactions, the K^+-ion insertion and extraction kinetics are much faster and the reversibility of the phase transformation should be greater.

For example, Wu's group employed a 2D layered MoS_2 as a host material for potassium ion intercalation within the electrochemical window of 0.5 to 2 V.[126] According to CV results and XRD characterizations, a stable stoichiometric K^+-ion intercalation compound, $K_{0.4}MoS_2$, was found to store potassium through highly reversible K^+-ion intercalation and de-intercalation reactions in an electrolyte comprising 0.5 M KPF_6 dissolved in PC/ethylene carbonate (EC) (volume ratio [V_{PC}/V_{EC}] = 1:1). This compound generated in the first stage of potassium intercalation (around 1.02 V), and further intercalation at ca. 0.8 V leads to the formation of K_xMoS_2 ($x > 0.4$), but the continuous accumulation of this material induces the degradation of MoS_2 to potassium sulfides (K_xS), resulting in the loss of structural integrity of MoS_2. Thus, the discharge depth was set to 0.5 V to ensure that $K_{0.4}MoS_2$ is the only discharge product for participation in the subsequent redox reactions.

Unlike MoS_2, $K_{0.4}MoS_2$ exhibits a quite limited expansion of 34% along the c-axis in the potassiated state, even less than K^+-ion-intercalated graphite (ca. 67%). The excellent preservation of the structure endows this compound with a very steady cycling behavior; namely, its reversible specific capacity of 63.8 mAh g^{-1} is retained after 200 cycles with a capacity retention of 97.5%. Further, the discharge/charge profiles almost overlapped during cycling, and the corresponding CEs remained above 99.2%, well illustrating the high reversibility. In addition, Shu's group reported that pretreated commercial $TiSe_2$ could be used as an insertion-type anode for PIBs.[89] They employed in situ XRD measurements to investigate the potassiation and depotassiation mechanisms of $TiSe_2$ in the voltage range of 1.0 to 3.0 V (Figure 5A,B). The (002) reflections were unrecoverable, and this was ascribed to the insertion of K^+ ions into the vacant spaces between the van der Waals layers of $TiSe_2$, resulting in the separation of $TiSe_2$ and phase transformation instead of lattice strain in the first cycle. The first discharge process to 1.0 V resulted in the formation of $K_{0.8}TiSe_2$, and, subsequently, $K_{0.24}TiSe_2$ was produced after full recharging to 3.0 V, resulting in some capacity loss during the incomplete depotassiation reaction. This newly formed $K_{0.24}TiSe_2$ phase has been shown to serve as a stable K^+-ion-intercalating host material for reversible potassium storage in an electrolyte comprising 0.8 M KPF_6 in diethylcarbonate (DEC) and EC (V_{DEC}/V_{EC} = 1:1). The oscillation between $K_{0.24}TiSe_2$ and $K_{0.8}TiSe_2$ proceeds in the subsequent cycles, as shown in Figure 5C,D.
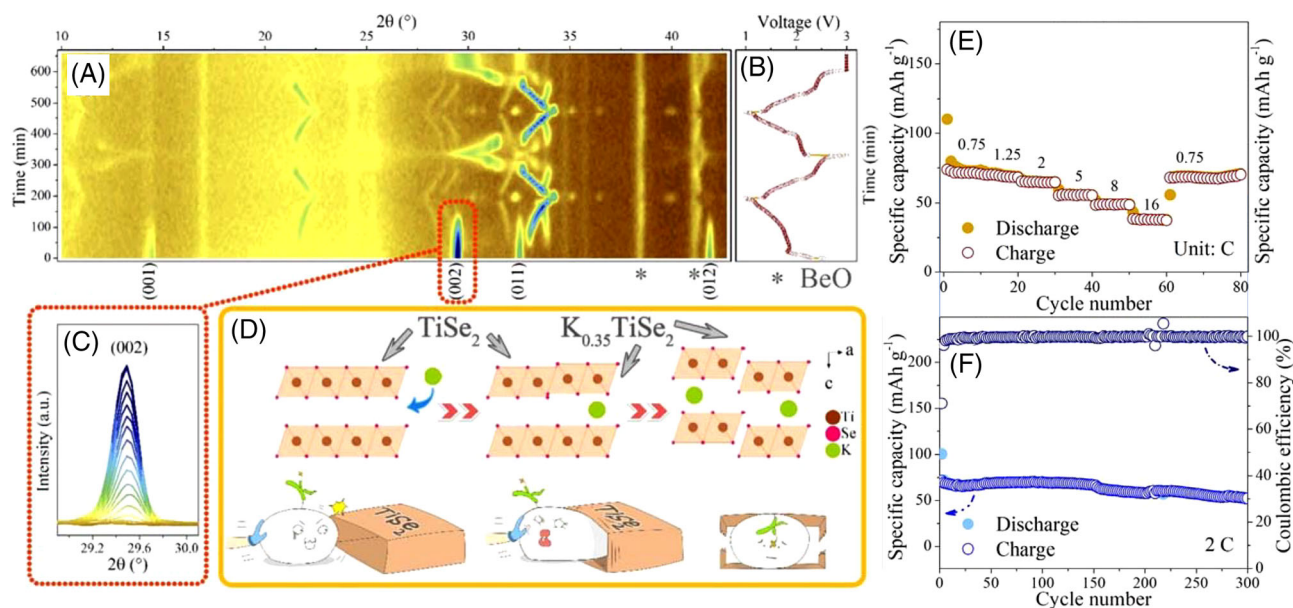

FIGURE 5 A, In situ XRD image plots; B, corresponding discharge/charge curves; C, intensity evolution of the (002) diffraction peak; and D, schematic illustrating structural evolution of $TiSe_2$ upon potassiation and depotassiation. E, Rate capability and F, cycling behavior of $TiSe_2$ over the voltage window of 1 to 3 V. Reproduced with permission from Reference 89 Copyright 2019, Elsevier

Fortunately, fast reaction kinetics (72.6 mAh g^{-1} at 0.75C and 38.3 mAh g^{-1} at 16C) coupled with decent cycling stability (300 cycles at 2C) were synchronously achieved in this case (Figure 5E,F). After solving the irreversible capacity loss by using pretreatment cycles, TiSe$_2$ (K$_{0.24}$TiSe$_2$, more precisely) was matched with pretreated Prussian blue to construct a full-cell PIB with high initial CE (ICE) and stable cycling performance.

However, it is noteworthy that the cycling stability is improved at the sacrifice of the specific capacity under this circumstance. Approximately at least two-third of the capacity for potassium storage arises from the conversion and alloying reactions of the metal chalcogenides.[103,108] Thus, limiting the discharge depth to intercalation reaction cannot take advantage of this dominant portion of the theoretical capacity. It also needs to point out that the relatively high discharge voltage plateau of intercalation reactions will reduce the working voltage and energy density of assembled full-cell PIBs.

2.3.2 | Nanostructure engineering

Considering that the intrinsically low electric and ionic conductivities in the bulk are already one of the most critical hindrances to the use of metal chalcogenides as efficient potassium ion host materials at high rates, nanostructure engineering should be an effective strategy to promote their reaction kinetics by quantum confinement effects, which means a distinctly higher utilization of active materials and a larger potassiation/depotassiation depth.[2,7,127] Besides, constructing nanostructures not only helps shorten ion diffusion pathways and facilitate electron transfer, but also self-accommodates volume change during discharge and recharge cycles, alleviating the electrochemical collapse caused by mechanical stress. As a result, the potassium storage capability of nanostructured metal chalcogenides has been significantly enhanced, especially in terms of capacity and cycling performance.

A range of specially designed metal-chalcogenide-based nanostructures have been successfully synthesized until now having, for example, wide coverage of nanoparticles (zero-dimensional [0D]), nanotubes (one-dimensional [1D]), nanosheets (2D), and interconnected porous networks (three-dimensional [3D]). The preparation methods mainly involve hydrothermal/solvothermal growth, chemical vapor deposition (CVD), high-temperature calcination, hard/soft templating, or various combinations of these techniques.

Wang's group has published several interesting works related to this research direction. First, they prepared a flexible freestanding anode consisting of metallic octahedral CoSe$_2$ threaded with N-doped carbon nanotubes for PIBs through solvothermal growth and selenylation (Figure 6A).[20] These octahedral CoSe$_2$ nanoparticles with an average size of 150 to 200 nm are highly dispersed along the carbon tubes in sequence, thus providing sufficient void space to buffer the volume expansion upon potassiation and improve the structural stability during cycling (Figure 6B,C). Benefiting from the synergistic effect of the fast electron transfer of nanosized CoSe$_2$ itself and the unique hierarchical structural advantages of the composite, this freestanding CoSe$_2$-based framework demonstrated superior electrochemical performance when tested as a PIB anode in 0.8 M KPF$_6$ + DEC/EC (vol/vol = 1:1) electrolyte. A stable reversible capacity as high as 296 mAh g^{-1} was obtained with this hybrid anode at 0.2 A g^{-1}, and there was more than a two-third capacity contribution at voltages below 0.5 V (Figure 6D). Further, when the current density was increased from 0.2 to 2 A g^{-1}, the material exhibited a high capacity retention of ca. 68%. What is more attractive is its excellent long-term cycling stability. The electrode could be operated steadily for 600 cycles at 2 A g^{-1} and showed negligible capacity loss even after the last cycle (Figure 6E). Furthermore, the phase transformation of CoSe$_2$-Co$_3$Se$_4$-(Co$_3$KSe$_4$ + CoSe)-(Co + K$_2$Se) explained as the detailed potassiation procedure via first-principle calculations. Next, a unique nanostructure of bamboo-like hollow MoS$_2$/N-doped C tubes, as displayed in Figure 6F, was reported by their group.[90] These hybrid tubes mainly consist of MoS$_2$ (ca. 75 wt%). Interestingly, the distance between the adjacent (002) planes of MoS$_2$ reached 10 Å in the tubes because of the presence of carbon interlayers, proven by Figure 6G,H. The expanded MoS$_2$ layers with abundant defects could provide more active sites for potassium storage, as well as more channels for ion diffusion, which is significant for reducing the ion migration energy barrier and then improving reaction kinetics. The special 1D hollow microstructure endows the composite with high stability, given that the mechanical stress can be gently released because the volume change is along the direction of tube walls. The high capacity of 451 mAh g^{-1} coupled with outstanding cycling stability (74% capacity retention after 1000 cycles) is evidence of these favorable features (Figure 6I,J). It is worth noting that, even when the scan rate was increased to 1.1 mV s^{-1}, faradaic pseudo-capacitance contributed to 73% of the capacity, which is unlike the situation in carbon-based materials (>90%). Density functional theory calculations were used to illustrate the merits of K$^+$-ion adsorption in MoS$_2$ with N-doped C interlayers compared to bulk MoS$_2$. A further modification to construct 3D interconnected MoS$_2$ networks has been carried out by Wang's group.[53] The nanosized rose-like MoS$_2$ anchored on reduced graphene oxide (rGO) was easily fabricated by a one-step hydrothermal method. The chemical Mo-C and Mo-O-C bonds guarantee the intimate interfacial
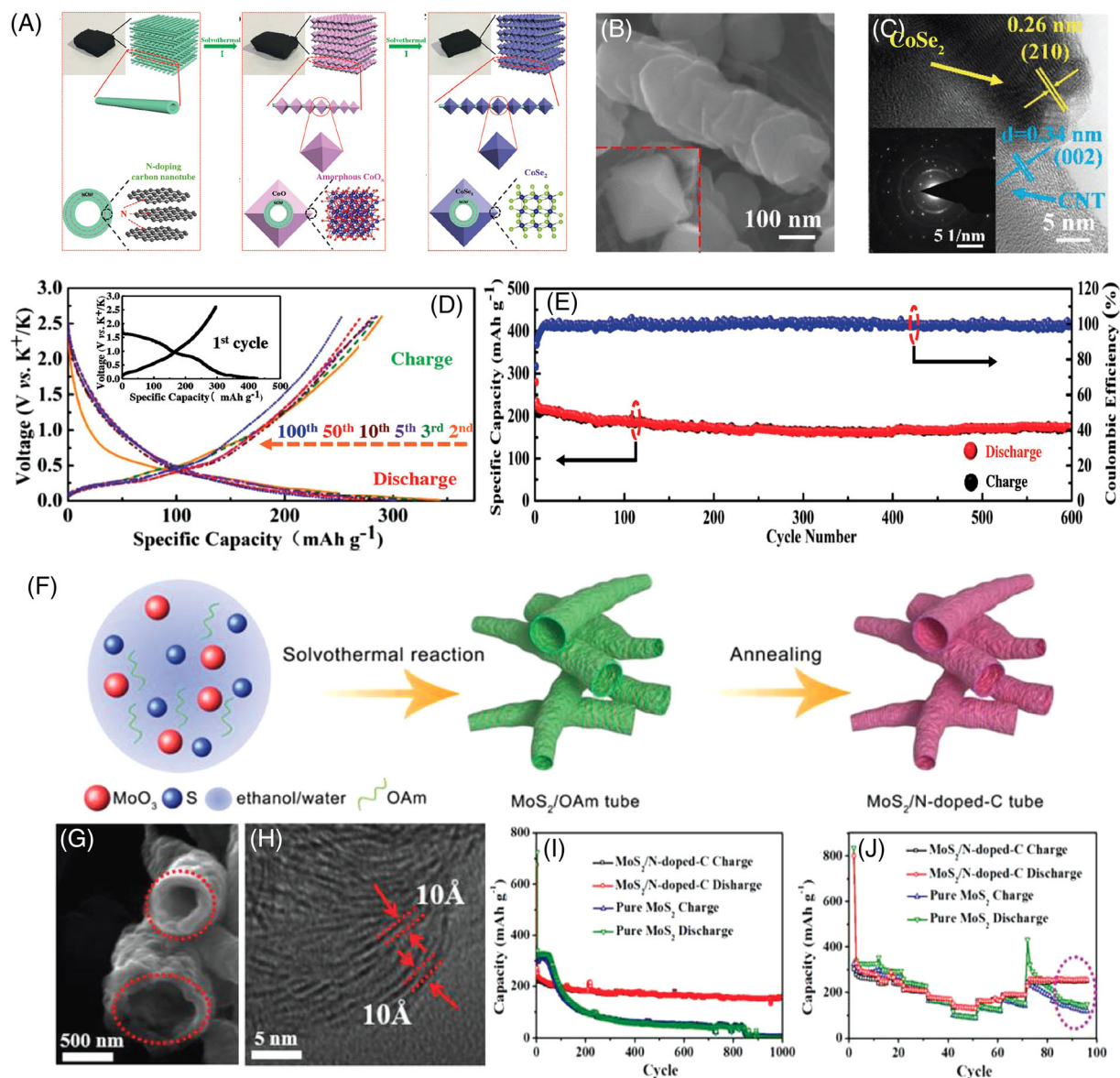
FIGURE 6 A, Schematic illustrating the fabrication procedure; B, scanning electron microscopy (SEM); and C, HRTEM images of NCNF@CS-6h. D, The selected charge/discharge profiles at 0.2 A g^{-1} and E, long-term cycling stability at 2.0 A g^{-1} of NCNF@CS-6h for potassium ion batteries (PIBs). Reproduced with permission from Reference 20 Copyright 2018, Wiley-VCH. F, Synthesis process; G, SEM; and H, HRTEM images of the porous MoS$_2$/N-doped-C tube. I, Cycling performances and rate capability of pure MoS$_2$ and MoS$_2$/N-doped-C tube. Reproduced with permission from Reference 90 Copyright 2018, Wiley-VCH

connection between MoS$_2$ and rGO. Simultaneously, the 3D interconnected networks provide abundant electron transfer and ion migration channels and alleviate the agglomeration of the 2D nanosheets caused by van der Waals interactions during cycling. The above features give this nanosized rose-like MoS$_2$ outstanding rate and cycling behavior. More surprisingly, only 46.2% of the capacity is contributed by pseudocapacitance even at 1 mV s^{-1}; thus, the high capacity retention at high rates is mainly achieved by the diffusion-controlled bulk conversion reactions, which provide a much larger contribution to the capacity than surface pseudocapacitance.

Of course, it also deserves to highlight several other representative works in this research area. Guo's group utilized hollow carbon spheres as a hard template to anchor few-layered V$_5$S$_8$ nanosheets directly on the surface through solvothermal growth and a subsequent phase transformation step via high-temperature annealing.[81] On the one hand, the 2D ultrathin structure greatly shortens the ion transport pathway, enabling a faster conversion reaction. On the other hand, ultrathin V$_5$S$_8$ nanosheets can be tightly pinned on the carbon nanospheres, thus self-confining the volume change, enhancing the structural stability, and preventing the

aggregation of nanosheets. Hence, a high reversible capacity of 645 mAh g^{-1} was achieved at 0.05 A g^{-1}, and around 190 mAh g^{-1} was retained after 1000 cycles at 2 A g^{-1} without obvious capacity decay compared to the initial cycle. In addition, the capacity of 153 mAh g^{-1} at 10 A g^{-1} achieved by V_5S_8/carbon hollow spheres is the best rate capability among all reported metal-chalcogenide-based PIB anodes to date.

The original investigation of Sb_2S_3 nanosheets for PIBs was also conducted by Guo's group.[55] They produced few-layered Sb_2S_3 nanosheets with an amorphous carbon coating via solution-triggered one-step shear exfoliation of bulk Sb_2S_3 in water/ethanol solvent. The as-prepared Sb_2S_3 nanosheets delivered a large reversible capacity of approximately 500 mAh g^{-1} at 0.05 A g^{-1} and demonstrated better cycling performance in $KSiF_6$ + EC/PC (vol/vol = 1:1) electrolyte than bulk Sb_2S_3. The main reason for the difference lies in the fact that the soft 2D microstructure of the Sb_2S_3 nanosheets not only boosts ion diffusion along short pathways but also enables the reversible recovery to the original structure by buffering and self-accommodation of the volume changes, whereas bulk Sb_2S_3 is easy to suffer from cracking and pulverization during cycling. In addition, Lu's group synthesized a flower-like nanostructure assembled from $MoSe_2$/N-doped carbon nanosheets ($MoSe_2$/N-C)[96] in which only a small number of amorphous N-doped carbon layers are attached to $MoSe_2$ nanosheets. In contrast to pure $MoSe_2$ blocks, $MoSe_2$/N-C shows an obviously higher and more stable capacity during cycling, demonstrating the promise of nanostructure engineering. Xia's group reported a novel kind of PIB anode material comprising few-layered SnS_2 supported on rGO.[93] Similarly, the nanostructured SnS_2 architecture delivered a higher reversible capacity of 448 mAh g^{-1} and longer working lifetime of up to 300 cycles. It should be emphasized that nearly 73% (325 mAh g^{-1}) of the entire capacity is obtained in the voltage range of 0.01 to 0.5 V, which is more superior to those of most previously reported anode materials. Thus, this result demonstrates a significant step toward high-energy-density full-cell PIBs to some extent.

Although the aforementioned works reveal the positive aspects of nanostructure engineering, some unfavorable influence is worth our reconsideration as well. First, it is recognized that nanosized active materials have a low tap density. This is a critical performance index for industrial-grade products, and a low tap density makes it hard to guarantee the volumetric energy density of the electrode. Second, nanostructured materials expose more surface areas while having higher chemical activity at the same time. Therefore, how to generate a thin, stable, mechanically strong, and continuous SEI film with high ionic conductivity on the material surface remains a significant challenge. Thirdly, a larger SEI will mean greater consumption of K^+, thus increasing the irreversible capacity and reducing the ICE if without other modification techniques. Finally, aside from the buffering effect, the problem of structural instability has not been addressed thoroughly. In particular, metal-chalcogenide-based nanostructures always lack a physical or chemical barrier to prevent the pulverization of active components.

2.3.3 | Confinement by carbon nanophases

Because of its high structural stability and lightweight, carbon nanophases have already been combined with metal chalcogenides to prepare novel composites for applications requiring high structural stability. Fortunately, this traditional modification strategy, which has been used for LIBs and SIBs, is also effective for PIBs and allows the improvement of the electrochemical performance. On the one hand, carbon nanophases can play a role of soft barrier to confine the volume changes and self-aggregation of the metal chalcogenides during potassiation and depotassiation, significantly enhancing the tolerance to structural damage. On the other hand, the carbon matrix is also able to supply high-speed electron transfer pathways to the dispersed metal chalcogenides, thus improving the electrical conductivity of the composites. Two forms of confinement by carbon nanophases have been used for metal chalcogenides. In one, tiny metal chalcogenides are embedded into carbon matrix directly, and the volume expansion is restricted by the internal stress of carbon phase. The other is to encapsulate metal chalcogenides in carbon nanophases with void spaces, allowing controllable volume expansion within a restricted region.

Obviously, the former method is easier to realize in terms of material preparation. Electrospinning is widely used to construct composites of metal chalcogenides embedded in carbon. For example, Zhang's group prepared graphene-encapsulated FeS_2 nanoparticles embedded in carbon nanofibers (FeS_2@G@CNF) through electrospinning and calcination.[80] The introduction of graphene facilitated the uniform distribution of ultrafine FeS_2 nanoparticles in the carbon nanofibers, and there was little FeS_2 at the surface zone of the nanofibers. When evaluated as the anode material for PIBs, FeS_2@G@CNF exhibited acceptable cycling stability over 680 cycles (ca. 62% capacity retention), even though some capacity decay was observed within the initial 100 cycles. Qian's group used a similar strategy to prepare ultrafine $VSe_{1.5}$ nanoparticles embedded in carbon nanofibers.[95] In this composite, the $VSe_{1.5}$ nanoparticles are closely

surrounded by disordered carbon, which effectively confines the migration or aggregation of $VSe_{1.5}$ during cycling, as shown in Figure 7A,B. Although only the data from the initial 100 cycles was provided, the capacity was maintained at around 177 mAh g^{-1} at 1 A g^{-1} (Figure 7C). Zhang's group specially designed 3D amorphous carbon-coated CoS/N-doped CNTs anchored on CoS-coated carbon nanofibers as an anode material for PIBs. The composite was prepared by electrospinning, seed-assisted growth, in situ CVD, and high-temperature sulfuration.[94] Some of the CoS nanoparticles with an average diameter of ca. 20 nm were encapsulated at the ends of the CNTs, whereas the remainder was anchored on the surface of the amorphous N-doped carbon nanofibers. Benefiting from confinement effects, this electrode demonstrates a stable capacity of nearly 400 mAh g^{-1} and decent cycling stability of up to 600 cycles at 3.2 A g^{-1}. However, the material showed severe capacity loss in the first 100 cycles, possibly
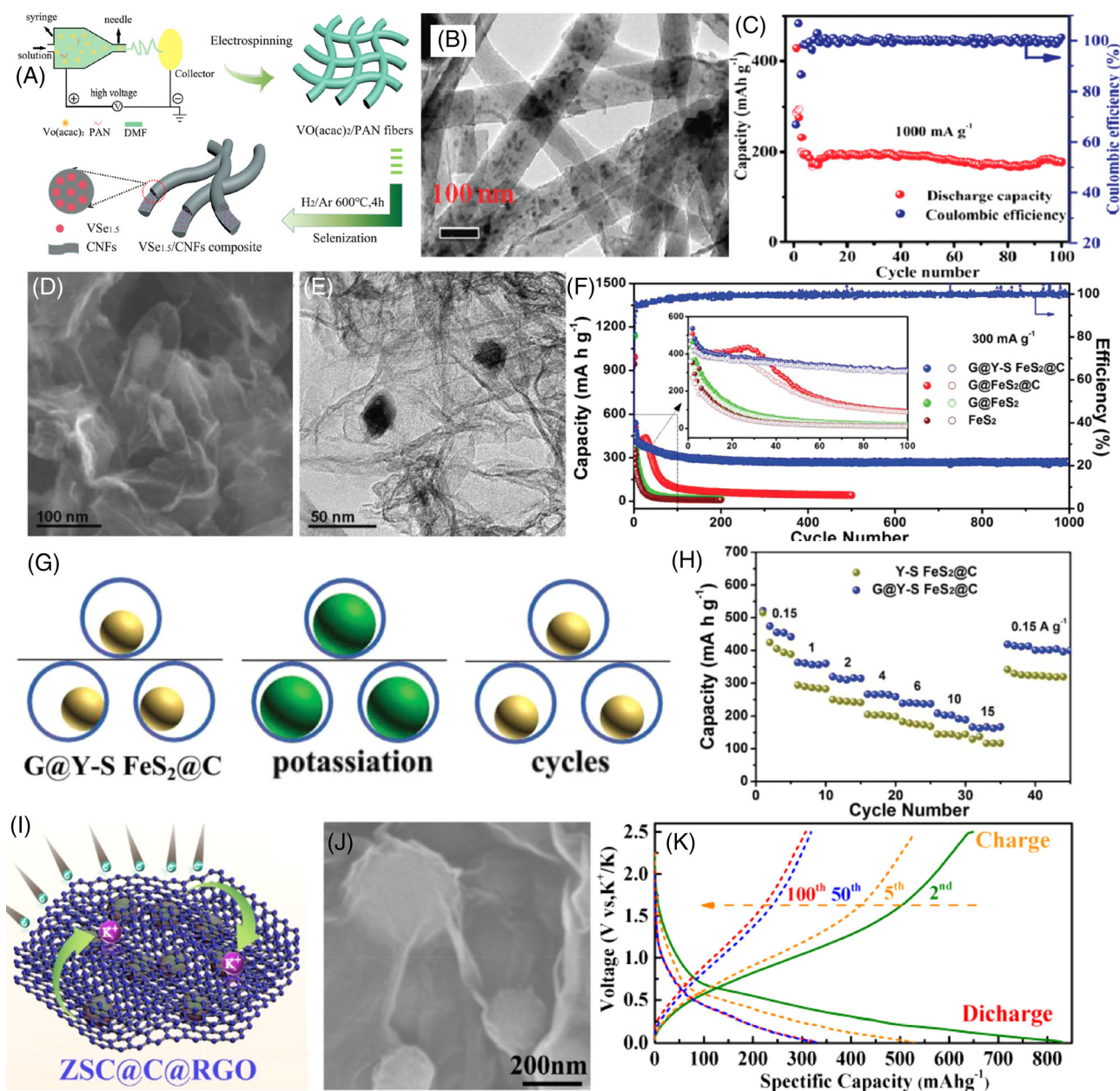

FIGURE 7 A, Schematic for the synthesis; B, transmission electron microscopy (TEM) image; and C, cycling performance of $VSe_{1.5}$/CNF composite for potassium ion batteries (PIBs). Reproduced with permission from Reference 95 Copyright 2019, The Royal Chemical of Society. D, Scanning electron microscope (SEM) and E, TEM images of G@Y-S FeS$_2$@C. E, Cycling performance of G@Y-S FeS$_2$@C, G@FeS$_2$@C, G@FeS$_2$, and FeS$_2$. Reproduced with permission from Reference 92 Copyright 2018, Wiley-VCH. I, Schematic illustration of the microstructure; B, SEM image; and K, galvanostatic charge/discharge profiles at 0.05 A g^{-1} of ZSC@C@RGO. Reproduced with permission from Reference 56 Copyright 2019, American Chemical Society

due to the activation process, as well as the collapse of unstable components without carbon protection.

In contrast, the latter confinement strategy using nanocarbon with void spaces seems to be more efficient in maintaining the structural stability of composites during potassiation and depotassiation cycles. However, the microstructure and corresponding preparation procedure requires innovative and careful design. The yolk-shell structure is one of the most promising candidates in this kind of modification strategy, providing suitable void space for metal chalcogenides to accommodate their volume expansion, but this expansion is seriously restricted in the "shell"-protected area. Thus, very little mechanical stress caused by volume expansion will be imposed on the carbon shell, and the pulverization of metal chalcogenides will be significantly alleviated within the nanoconfined space. Thus, the structural stability coupled with ion/electron transfer kinetics of the whole composite are highly improved. An impressive work reported by Guan's group is worth highlighting here.[92] They synthesized a yolk-shell $FeS_2@C$ nanostructure anchored on a graphene matrix. The controllable volume change of FeS_2 happens inside the carbon shell while the intercrossed graphene connects those yolk-shell $FeS_2@C$ units to ensure the high conductivity and sufficient structural stability (Figure 7D,E,G). When tested in 1 M KPF_6 + EC/PC (vol/vol = 1:1) electrolyte, the composite delivered a stable capacity of around 100 mAh g^{-1} over 1500 deep cycles at a high rate of 5 A g^{-1} (Figure 7F,H). Guan's group also prepared a 0D/2D hybrid structure comprising yolk-shell $NiS_x@C$ embedded in carbon nanosheets (Y-S $NiS_x@C$).[111] In this composite, numerous $NiS_x@C$ and carbon nanocage units with an average size of ca. 30 nm were homogeneously embedded in a carbon nanosheet matrix. Under the double protection of the carbon "shell" and carbon nanosheets, the Y-S $NiS_x@C$ achieved an ultralong cycling stability of 8000 cycles, and, surprisingly, the capacity was maintained at approximately 130 mAh g^{-1}. Furthermore, the unique microstructure was well maintained after cycling tests. Not limited to this, Bao's group designed another double protective structure for ZnS, where hybrid microspheres assembled from ZnS nanorods and an amorphous carbon coating were sandwiched between rGO layers.[56] There are enough voids between the ZnS/C microspheres and rGO substrate to buffer the volume expansion of ZnS. The amorphous carbon coating acts as the first protective layer, holding ZnS nanorods together like binders, whereas the second protective rGO layer limits the aggregation or pulverization of the ZnS/C microspheres and offers fast pathways for electron transfer, as illustrated in Figure 7I,J. Hence, stable cycling behavior for over 300 cycles was obtained, after some initial activation cycles, as displayed in Figure 7K.

Consequently, confinement using carbon nanophases shows better feasibility in improving the electrochemical performance of metal chalcogenides, especially the long-term cycling stability at high rates. It is still worth noting that the excess consumption of K^+ ions caused by SEI formation leads to an obvious decrease of ICE, on account of the introduction of porous or amorphous carbon nanophases. Moreover, metal chalcogenides commonly exist in carbon nanophases in the form of nanosized structures; thus, an inadequate tap density is another issue of concern.

2.3.4 | Ternary alloying

The ternary alloying method is a new concept for metal chalcogenides modification proposed in recent years. It can take care of both the aforementioned problems concerning tap density and electrochemical performance. The main aim of this modification is to enrich the material with vacancies, adjust the electronic structure, and optimize the physical properties of metal chalcogenides by introducing a third-party cation (metal atom) or anion (chalcogen), which helps to increase the number of active sites, facilitate reaction kinetics, and alleviate the structural vibrations of ternary metal chalcogenides.

Guo's group has pioneered the design, synthesis, and structural/electrochemical investigations of ternary metal chalcogenides that are suitable for PIB anodes. They fabricated $MoS_{2(1-x)}Se_{2x}$ alloys (x = 1, 0.75, 0.5, 0.25, and 0) by replacing Se atoms with S atoms in $MoSe_2$ nanoplates via a facile alloying approach.[112] They found that an S/Se ratio of nearly 1:1 endows the alloys with the largest vacancy concentration. These vacancy sites not only boost electron transfer but reduce the K^+-ion adsorption energy barrier and alleviate structural change during cycling (Figure 8A-D). When used as a PIB anode material, the MoSSe alloy delivered a high reversible capacity of 517.4 mAh g^{-1} at 0.1 A g^{-1} and good cycling stability (220.5 mAh g^{-1} after 1000 cycles at 2 A g^{-1}), as shown by the electrochemical performance illustrated in Figure 8E-G. They also prepared another ternary metal chalcogenide ($SnSb_2Te_4$) through the substitution of cations.[97] To improve the electric and ionic conductivity of the $SbSb_2Te_4$ p-type topological insulator, nanodots were dispersed in a few-layered graphene substrate by a facile ball-milling method. The reaction kinetics is accelerated by the PN heterojunction and the conductive topological surface, and excellent potassium storage was achieved in 1 M potassium bis(fluorosulfonyl)imide (KFSI) + DMC electrolyte. Furthermore, Wang's group also reported few-layered ternary chalcogenide Ta_2NiSe_5

nanosheets for PIBs.[91] Ion-intercalation-mediated exfoliation yields Ta_2NiSe_5 nanosheets with an expanded interlayer distance of 1.1 nm, as well as abundant Se sites originating from the $NiSe_4$ and $TaSe_6$ octahedral clusters. The above features are favorable for potassium storage so that they can demonstrate a large capacity of 315 mAh g^{-1} with a moderate ICE of 70%, decent rate capability (121 mAh g^{-1} at 1 A g^{-1}) and stable cyclability (81.4% capacity retention after 1100 cycles).

Thus, research to date indicates that ternary alloying is a very promising modification strategy for metal chalcogenides on basis of known research findings. However, current investigation into the alloy categories, physical structures, and electrochemical mechanisms is far from adequate. It is believed that more suitable ternary metal chalcogenides for high-performance PIBs will be developed if more insights are revealed in this direction.

2.4 | Regulating the electrolyte for metal chalcogenides

Compared with electrode material modification, optimization of the electrolyte has drawn less attention from researchers in PIB research. However, due to the high activity of K^+-ion-based electrolytes, the appropriate pairing of potassium salt and solvent is a critical step for constructing moderate SEI layers, reducing parasitic reactions, and maintaining structural stability. However, research into this topic began late and is still in infancy. Despite several kinds of electrolytes have already been used for PIBs (mainly KPF_6, KFSI, or potassium bis(trifluoromethane) sulfonimide as solutes and employing EC/DEC, EC/PC, or dimethoxyethane [DME] as solvents), but their effects on the electrochemical performance of a certain metal chalcogenide have usually been neglected. To date, very few attempts at optimizing the electrolyte component of
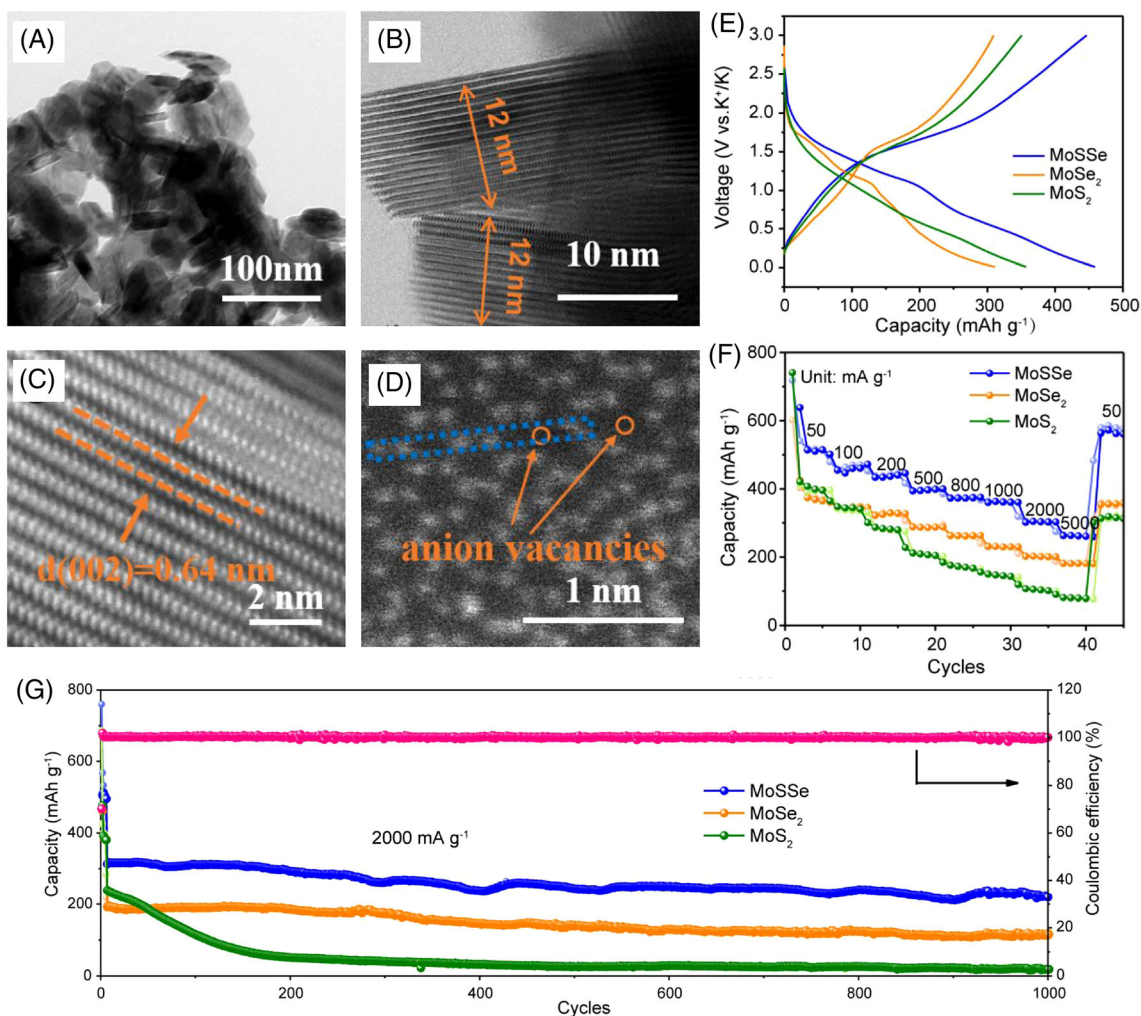

FIGURE 8 A, STEM; B, HRTEM; and C,D, magnified HRTEM images of MoSSe. E, Charge/discharge profiles at the fifth cycle; F, rate capability; and G, cycling performance for $MoSe_2$, MoSSe, and MoS_2. Reproduced with permission from Reference 112 Copyright 2019, American Chemical Society

metal-chalcogenide-based PIB anodes have been reported.[96,97]

For example, Lu's group studied the effect of four kinds of electrolytes on the cycling behaviors of MoSe$_2$ nanosheets.[37] When a 1 M KPF$_6$ + DME electrolyte was employed, the battery stopped functioning suddenly in the 13th cycle. In the cases of 1 M KPF$_6$ + EC/DEC (vol:vol = 1:1) and 1 M KPF$_6$ + EC/DMC (vol:vol = 1:1) electrolytes, rapid capacity decay occurred over the first 100 cycles. In contrast, MoSe$_2$ nanosheets maintained stable cycling in 1 M KFSI + EMC and 3 M KFSI + DME electrolytes, but the reversible capacity was slightly higher in the former electrolyte. The authors hypothesized that the more stable SEI formed by KSFI is responsible for the long cycling stability (Figure 9A). Guo's group investigated the electrochemical performance of SnSb$_2$Te$_4$ nanodots in KFSI + DMC or KSFI + EC/DEC electrolytes.[97] The SnSb$_2$Te$_4$ nanodots delivered very stable capacities of around 320 mAh g^{-1} over 200 cycles in the KFSI + DMC electrolyte, whereas an obvious capacity decrease began after the 120th cycle in the KFSI + EC/DEC electrolyte. The galvanostatic cycling profiles of symmetric foil cells in different electrolytes indicate

that K foil shows the lowest voltage hysteresis in the KFSI + DMC electrolyte (Figure 9B,C). The stability of the K foil is regarded as the main reason for the longer cycling lifetime.

The above attempts illustrate the important role of the electrolyte in achieving high-performance metal-chalcogenide-based PIB anodes. However, the underlying mechanisms and general design principles need more detailed explorations to specify.

3 | METAL CHALCOGENIDES FOR POTENTIAL POTASSIUM STORAGE SYSTEMS

In addition to the widely investigated PIBs, potassium-sulfur/selenide batteries, potassium-ion capacitors, and potassium-oxygen batteries have emerged as novel types of potassium-based energy storage media due to the relatively high energy densities.[128-130] Recently, the intriguing electronic properties of metal chalcogenides make this category of materials available for the above applications. In this section, we briefly discuss the progress and
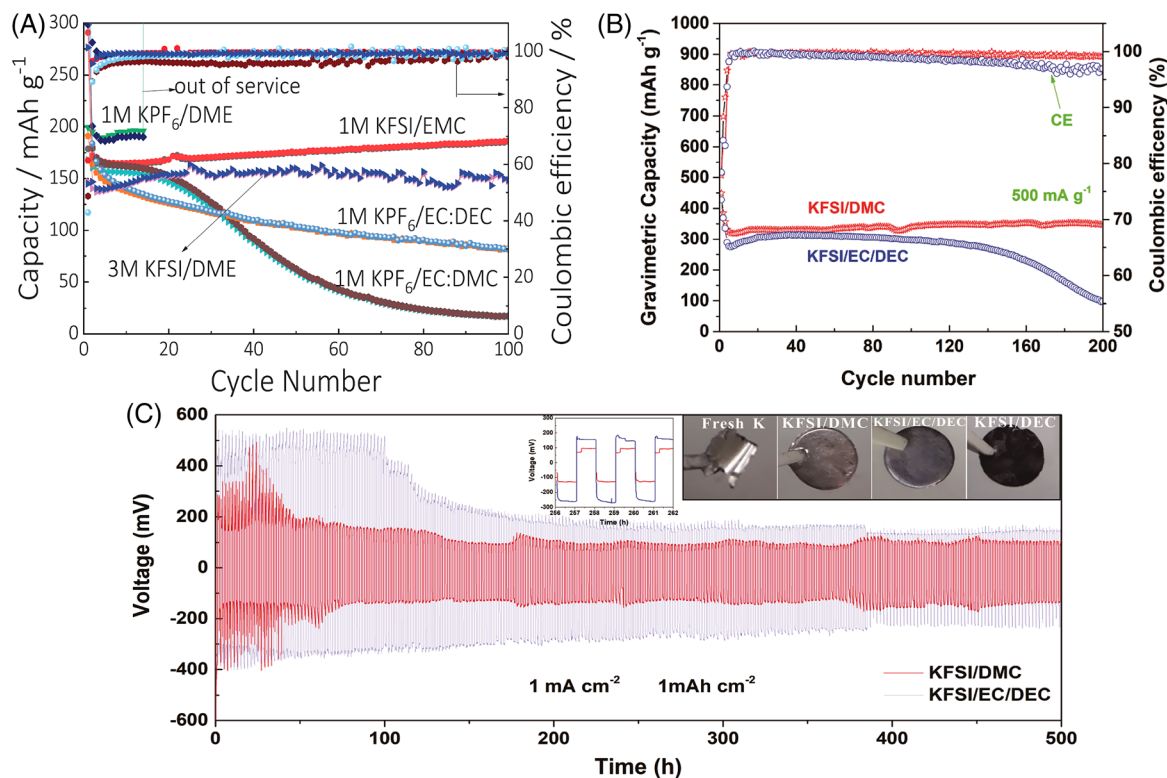

FIGURE 9   A, Cycling performance of MoSe$_2$/N-C in different electrolytes at 1 A g^{-1}. Reproduced with permission from Reference 37 Copyright 2018, Wiley-VCH. B, Cycling performance of SnSb$_2$Te$_4$/G for PIBs at 0.5 A g^{-1} with different electrolytes. (d) Galvanostatic cycling of symmetric foil cells in different electrolytes at 1 mA cm^{-2} with a stripping/plating capacity of 1 mAh cm^{-2}. The magnified voltage-time profiles and digital photos of K immersed in different electrolytes are inset. Reproduced with permission from Reference 97 Copyright 2019, Wiley-VCH

possibilities of these novel potassium storage systems based on metal chalcogenides.

3.1 | Cathode stabilizers for K-S/Se batteries

Unlike the fundamental intercalation reactions in Li/Na/K^+-ion batteries, potassium-sulfur (K-S) and potassium-selenide (K-Se) batteries are based on the conversion or integration of potassium polysulfide/selenide analogs on the cathode. The performance of K-S/Se batteries is severely inhibited by three main factors as follows[128,131]:

1. The dissolution of potassium polysulfide/selenides and the shuttle effect, which result in the accumulation of potassium sulfides/selenides (obtained through the reduction of potassium polysulfide/selenides by highly reductive potassium) on the metal anode surface and blockage of K^+-ion diffusion channels from electrode to electrolyte.
2. The low utilization of the theoretical capacity caused by the weak electric and ionic conductivity of elemental sulfur/selenium.
3. Structural instability toward pulverization because of the large volume expansion and shrinkage of sulfur/selenium during repetitive potassiation and depotassiation processes.
4. The severe side reactions originating from the highly reactive potassium metal anodes.

At the present stage, efforts have been mainly focused on addressing the above issues facing sulfur/selenium cathodes according to recent reports. Carbon substrates with porous structures are mainly utilized as host materials to improve the ionic/electric conductivity of S/Se, as well as buffering their volume expansion upon discharging to enhance the structural stability. For example, sulfur can be stored in microporous carbon substrates via impregnation or vaporization-condensation methods. Xu's group has carried out an impressive work related to this.[100] In their studies, small allotropes of sulfur (S_n, $n \leq 3$) were confined in a microporous carbon matrix, which prevented the sublimation and decomposition of sulfur via the strong interactions between the fragment sulfur species and carbon atoms, thereby effectively alleviating the solvation of polysulfides and enhancing the reaction kinetics. This synergistic effect endowed this K-S battery with a reversible capacity of 1198.3 mAh g^{-1}, moderate CE of 97%, and good cycling stability, retaining 869.9 mAh g^{-1} after 150 cycles. By impregnating SeS_2 into an N-doped freestanding porous carbon nanofiber film, a self-supported SeS_2/C cathode was fabricated by Yu's group.[129] The encapsulation of nanosized SeS_2 into a carbon matrix not only minimized the volume expansion but shortened the ion transport pathways. Meanwhile, these interconnected carbon nanofibers also provide a highly conductive network for electron transfer. As a result of this synergistic effect, the electrode had an enhanced rate capability and extended cycling lifespan. Conductive polymers have also been used as host substrates for S/Se storage. Recently, Sun's group found that sulfurized polyacrylonitrile (SPAN) composites are promising cathodes for K-S batteries with polyacrylic acid (PAA) as a binder.[131] The PAA greatly improved the structural stability of the SPAN electrode because of the excellent cohesion of the active materials with the electrode, which increased its ability to accommodate the large volume expansion upon cycling. As a result, a high reversible capacity of 1050 mAh g^{-1} and good reversibility (95% capacity retention after 100 cycles) were achieved.

Whereas the lack of physical barrier around the electrolyte means that polysulfide/selenides can still be extracted from the host materials, dissolved in the electrolyte, and diffuse into the potassium anode, leading to little improvement in the cycling stability, as proved by the above works. Awareness of this issue has increased recently, and the construction of a protective layer around the active materials has been proposed as a solution. Chen's group used a coating of conductive polyaniline (PANI) on a CMK-3/sulfur hybrid cathode,[132] and this was found to promote the cycling performance significantly (62% capacity loss for pure sulfur compared to 28% for PANI-coated CMK-3/sulfur hybrid). Although the structure of the PANI-coated cathode was well preserved after 50 cycles, a few long-chain polysulfides were still shuttled to the metal side. Obviously, developing efficient physical barriers for advanced K-S/Se batteries is one of the most urgent tasks on the way to advanced K-S/Se batteries.

Inspired by the excellent protection against and adsorption of polysulfide/selenides by metal chalcogenides, we propose the possibility of them to be as efficient cathode stabilizers for K-S/Se batteries. This consideration is partially based on related works involving Li-S/Se and Na-S/Se batteries. For example, Jin's group synthesized Co_9S_8 nanocrystals with inlaid carbon (Co_9S_8/C) hollow nanopolyhedra derived from metal-organic frameworks using an impregnation method as a confinement barrier to host sulfur (S@Co_9S_8/C).[133] On the one hand, the large inner space of the Co_9S_8/C hollow nanopolyhedra ensured sufficient mass loading of S and accommodated the volume expansion of the Li_2S_x species. On the other hand, the polar Co_9S_8/C shells provided spatial confinement and chemical bonding to restrict the shuttling of lithium polysulfides. As a result of these favorable factors, the

S@Co$_9$S$_8$/C cathode yielded a high reversible capacity and very small capacity decay of 0.041% per cycle over 1000 cycles at 2C. Also conducted by Jin's group was interlaced carbon nanotubes threaded around hollow Co$_3$S$_4$ nanoboxes (CNT/Co$_3$S$_4$-NB) prepared by hydrothermal sulfuration.[134] The synergistic effect of ultrahigh charge transfer properties and physical/chemical confinement of Co$_3$S$_4$ nanoboxes meant that CNT/Co$_3$S$_4$-NB functioned as an efficient cathode stabilizer for Li-S batteries, which exhibited significant improvement in the electrochemical performance, especially in terms of long-term cycling stability. Metal chalcogenides are also capable of cathode stabilizers and catalysts in Na-S batteries. We specify this positive function by exemplifying two representative works employing MoS$_2$ and NiS$_2$, respectively. Xu's group prepared an S/MoS$_2$/C hybrid cathode by growing MoS$_2$ nanosheets on hollow carbon spheres as the S carrier for Na-S batteries.[135] The hollow carbon spheres provide space to host sulfur and improve its conductivity, and the MoS$_2$ nanosheets can effectively adsorb the soluble sodium polysulfide intermediates and alleviate the shuttle effect. Consequently, the cycling stability of this Na-S battery was extended to 1000 cycles. Dou's group synthesized N-doped CNTs implanted with NiS$_2$ crystals as a multifunctional sulfur host.[136] The polarized NiS$_2$ molecules not only immobilized the polysulfides by chemical adsorption but also facilitated the conversion of sodium polysulfides to Na$_2$S on discharging and S$_8$ on charging, as supported by the in situ synchrotron XRD results. These favorable features increased the battery's rate capability and lifespan to 750 cycles.

Although metal chalcogenides have not been utilized to host or stabilize potassium polychalcogenides in K-S/Se batteries until now to our best knowledge, it is believed that they can be easily extended into this field on account of the fact that their polar metal-chalcogen bonds and dangling chalcogen sites can efficiently adsorb polysulfides and accelerate the phase transformations in reported Li/Na-S batteries, as discussed above, thus greatly enhancing the specific capacity and cycling stability. Theoretically speaking, this stabilization strategy is considered to be equally effective in potassium storage systems such as K-S/Se batteries, which share a similar working mechanism.

3.2 | Potassium-ion capacitors

Having a similar electrode potential to Li$^+$/Li ($-$3.04 V vs SHE), K$^+$-ion hybrid capacitors (PICs) can be considered as an alternatives to lithium-ion hybrid capacitors (LICs) due to the higher abundance of K. However, the large radius of potassium ion (1.38 Å) results in sluggish redox kinetics in the anodes, which impedes their practical applications. To date, most research into PICs has been focused on carbon-based materials, such as carbon nanosheets, heteroatom-doped carbon, and porous hard/soft carbon, but there have been some attempts at using metal chalcogenides, which possess higher theoretical capacitances than carbon materials.

For example, KCu$_4$Se$_8$ nanowires with an average length of 30 mm were prepared by a modified composite-hydroxide-mediated approach and used in PICs by Sun's group.[137] The behavior of the PIC was studied by rotation electron diffraction, and the as-prepared KCu$_4$Se$_8$ were found to have a body-centered tetragonal structure. The capacitor assembled with the as-prepared KCu$_3$Se$_8$ electrode was tested under pressures of 0, 5, and 10 MPa, respectively, which showed that the optimal electrochemical performance was obtained at a scan rate of 5 mV s^{-1} and 0 MPa, yielding a specific capacitance of 25.3 F g^{-1}. Besides, the PIC also delivered an excellent long-term cyclability (112% of the initial capacitance after 5000 cycles) during continuous operation at 0.003 A cm^{-2}.

The recent work by Li's group verified that molybdenum diselenide (MoSe$_2$) is a promising anode material for PICs, where nitrogen-doped MoSe$_2$/graphene (N-MoSe$_2$/G) composites were prepared by a diatomite-templated method (Figure 10A).[98] SEM and TEM image analysis revealed that the bio-template approach endows the composite with a hierarchical structure. This unique microstructure offers a large number of openings and high porosity, thus increasing the interfacial contact as well as buffering the volume expansion during charge/discharge (Figure 10B-D). Sheet resistance (R_s) mapping of both composites revealed that the extra defects induced by the nitrogen doping effectively improved the electrical conductivity and, thus, enhanced the K$^+$-ion storage. Moreover, the adsorption sites for potassium atoms changed from the surface to the interlayer upon nitrogen doping. These results indicate that the potassium atoms are prioritized to be intercalated into the interlayers of N-doped MoSe$_2$, thus further enhancing the K$^+$-ion storage. When the as-prepared N-MoSe$_2$/G anode was matched with a bio-derived carbon cathode in a PIC device, a high-energy output (119 Wh kg^{-1}), satisfactory power delivery (7212 W kg^{-1}), and long lifespan of up to 3000 cycles were achieved. Thus, this PIC outperforms most reported counterparts (Figure 10E,F).

The successful construction of PICs reported above demonstrates that metal chalcogenides are a solid foundation as potassium host materials for PICs, having both high energy and power densities.
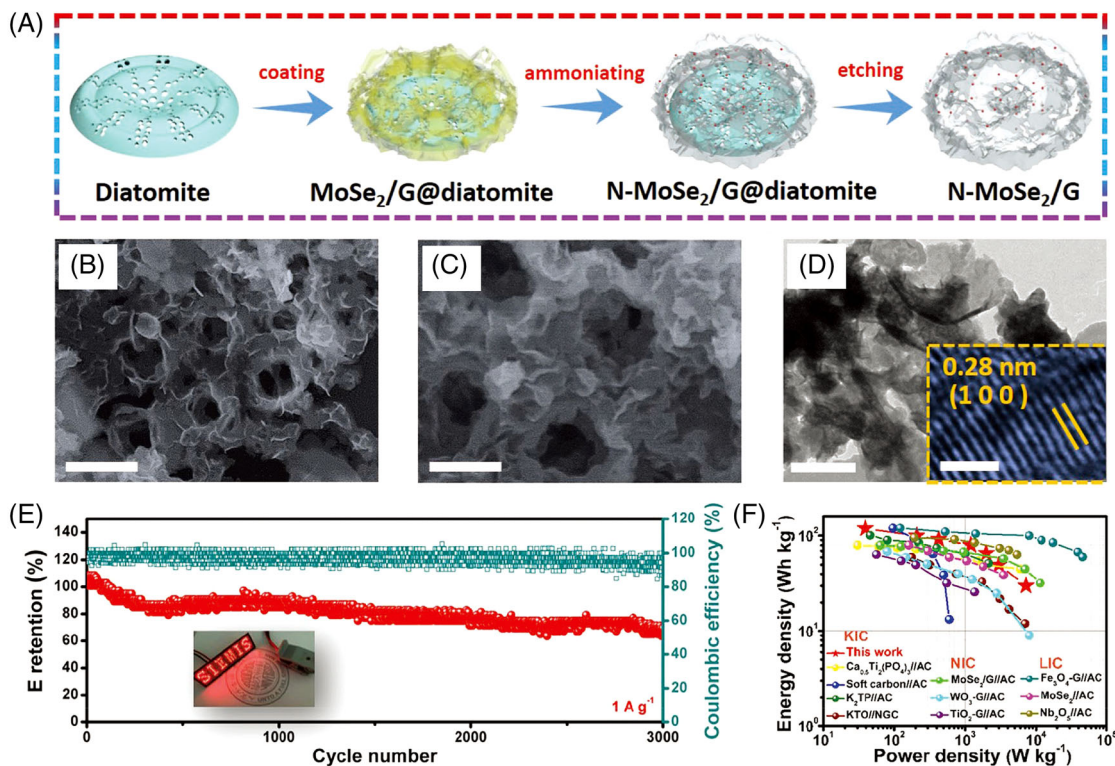
FIGURE 10 A, Schematic illustrating the preparation procedure; (B,C) scanning electron microscopy (SEM) images; and (D) transmission electron microscopy (TEM) image of N-MoSe$_2$/G. Scale bars: (B) 500, (C) 200, and (D) 200 nm. E, Cycling performance of the K$^+$-ion hybrid capacitor (PIC) using N-MoSe$_2$/G and bio-derived carbon. F, Comparison of electrochemical performances between N-MoSe$_2$/G and other typical materials for PICs. Reproduced with permission from Reference 98 Copyright 2019, Wiley-VCH

3.3 | Anode materials for potassium dual-ion batteries

The dual-ion battery (DIB) is a novel kind of energy storage system involving the separate intercalation of anions and cations into the electrodes during the charge/discharge process. The high working voltages (commonly above 4.0 V), low cost, and excellent safety of DIBs make them a worthy research field.[116,138] Among them, K-based DIB (PDIB) has emerged as a novel energy storage device within the last 3 years with the prosperity of PIBs. Like conventional PIBs, the electrochemical performance of PDIBs also relies on the potassium storage capability of anode material. In terms of existing anodes for PDIBs (such as K, Sn, and Pb),[139] there are often non-negligible problems concerning structural stability, capacity, reversibility, and safety. Thus, the development of high-performance anode materials is currently a hot topic. It is believed that the modified metal chalcogenides for PIBs can be easily transplanted to aid the research of PDIBs because they share a similar working principle and performance requirements in terms of the anodes that are responsible for reversible potassium storage.

In fact, this possibility has been partially supported by the successful application of metal chalcogenides (such as Ni$_3$S$_2$, WS$_2$, and MoS$_2$) as efficient and durable anodes for lithium (LDIBs) and sodium DIBs (SDIBs). For example, Bonaccorso's group verified the possibility of employing few-layer WS$_2$ flakes as lithium storage materials for LDIBs.[140] The WS$_2$ anodes were used in DIBs based on PF$_6^-$ and Li$^+$ insertion and yielded a charge capacity of 457 mAh g^{-1} and a wide cell voltage window of 0-4 V. Jiao's group used a 3D skeleton nanostructured Ni$_3$S$_2$/Ni foam coated with rGO as a high-performance DIB anode.[141] The assembled LDIBs operated in a voltage window of 4.2 to 4.5 V and showed excellent long-term cycling stability over 500 cycles with 85.6% capacity retention. In addition, MoS$_2$/N-doped carbon hollow spheres,[142] penne-like MoS$_2$/carbon nanocomposites,[143] and layer-by-layer stacked N,S-doped carbon/MoS$_2$ nanosheets[144] have also been fabricated for SDIBs using an NaPF$_6$ electrolyte. All exhibit stable cycling behavior but, notably, the reversible capacities are a little lower than those of LDIBs due to the lower sodium storage ability of metal chalcogenides.

On the basis of the aforementioned advances in the use of metal chalcogenides for DIBs, we believe high-performance PDIBs with metal-chalcogenide-based cathodes will be established as long as matching electrodes with suitable electrolytes and additives can be identified.

3.4 | Cathode catalysts for potassium-oxygen batteries

Alkali metal-O_2 batteries using aprotic electrolytes have received tremendous interest over the past decade because of their very high theoretical energy densities (eg, 3500 Wh kg^{-1} for Li-O_2 batteries and 350 Wh kg^{-1} for LIBs). Although alkali metal ions are not stored in the inner bulk of the cathode catalyst, they provide catalytic sites for the electrochemical reduction/oxidation of discharge products at the surface. Therefore, the catalysts play a key role in regulating the oxygen reduction reaction (ORR) and oxygen evolution reaction (OER) activities of air cathodes, for which the components and microstructures directly determine the final capacity, overpotential, and lifespan of metal-oxygen batteries. Among the various categories of catalysts for Li-O_2 batteries, metal chalcogenides have already been utilized to boost the reversible formation of Li_2O_2 on the cathode. For example, Yin's group utilized hierarchical $NiCo_2S_4$-based core-shell nanostructures as cathode catalysts for Li-O_2 batteries.[145] The specific capacity, discharge/charge reversibility, and cycling performance have all been improved. Kim's group employed NiS_2 nanosheets as cathode electrocatalysts, yielding a Li-O_2 battery with a lifetime of more than 300 cycles.[146] Other metal chalcogenide species have also proven to be beneficial for Li-O_2 batteries, such as $ZnCo_2S_4$,[147] $CoNi_2S_4$,[148] and $CuCo_2S_4$.[149]

Notably, compared to research into Li-O_2 batteries, that into K-O_2 electrochemistry is currently in the early stages. In fact, the ORR and OER mechanisms are much different in K-O_2 batteries.[101,130] KO_2 is believed to be the final stable discharge product (instead of K_2O_2, the potassium analog of the Li_2O_2 that is formed in Li-O_2 batteries). Some experimental results gave an evidence for this statement. For example, Wu's group proposed a K-O_2 battery based on O_2^--transfer on a carbon cathode.[130] In this system, first, the oxygen reacts with K$^+$ ions in the electrolyte to form KO_2 crystals, and, second, electrons migrate through the surfaces of the KO_2 crystals and react with oxygen and K$^+$ ions, enabling the growth of KO_2 from small crystals to nanosized particles and films. However, KO_2 rapidly covered the surface of the carbon cathode during the discharge process, resulting in an increased kinetic barrier due to the depletion of active sites exposed to oxygen. Besides, high currents also induced larger oxygen gradients on the porous carbon cathode, resulting in the less-efficient loading of discharge products. These are the key factors causing K-O_2 battery failure. Superior catalysts are expected to address the difficulties plaguing existing K-O_2 batteries.

On account of their enhanced electrocatalytic effects in Li-O_2 batteries, we think that metal chalcogenides will also be favorable for K-O_2 batteries. This consideration is mainly based on the following viewpoints. First, it is recognized that superoxides have a higher oxidizing ability than hyperoxides, so carbon electrode corrosion is more serious in K-O_2 batteries, which limits cyclability. Metal chalcogenides are effective electron donors, and the unpaired electrons from dangling chalcogen sites can neutralize the oxidizability of KO_2, reducing the structural damage and extending the longevity of the cathode catalysts. Second, the unoccupied 3d orbitals of transition metal atoms can act as mediators to accommodate the released electrons during the decomposition of discharge products and increase the fast transport of electrons from the electrode materials to the current collectors.

Generally, because these functions of metal chalcogenides have been demonstrated in the above aprotic Li-O_2 cases and other metal-O_2 batteries, where the cells with metal chalcogenide-based cathodes showed better electrochemical performance than their counterparts with pure carbon cathodes,[150-152] it is reasonable to further expect them to become cost-effective, efficient, and durable cathodes for K-O_2 batteries.

4 | SUMMARY AND PERSPECTIVE

Metal-chalcogenide-based composites exhibit great potential for potassium storage based on the findings of previous investigations. The depth of potassiation and depotassiation is strongly dependent on the reaction kinetics of metal chalcogenides, which is affected by their components, microstructure, particle size, and hybridization. Four dominant modification strategies including limitation of discharge depth, nanostructure engineering, confinement by carbon nanophases, and ternary alloying can be used to resolve the intrinsic structural instability and low electric/ionic conductivity of metal chalcogenides, which enable obvious improvements in electrochemical performance. However, these modification strategies still raise questions worth consideration. In the end, based on our thinking, the following points should receive more attention in future research focusing on metal chalcogenides for potassium storage.

1. Investigate the potassiation/depotassiation behavior of unrevealed metal chalcogenides. Despite several metal chalcogenides have already proven to be with electrochemical activity for PIBs, it cannot exclude the feasibility that those unexplored counterparts may demonstrate more superior potassium storage capability.
2. Construct more advanced metal-chalcogenide-based nanostructures or nanocomposites to facilitate long-term cycling stability at high rates. Multidimensional (such as 1D and 3D, 2D and 3D, and 0D and 3D)

metal chalcogenides are even more promising than those limited to a single dimension because of the combination of their corresponding advantages. Other highly conductive and ultrastable substrates besides carbon nanophases can be used for the hybridization of metal chalcogenides to enhance their structural stability and reaction kinetics.

3. Construct metal chalcogenide-based heterojunctions. This direction seems solely reported for metal chalcogenides-based PIB anodes. Nevertheless, surface/interface regulation should be an effective means that may direct the modifications to realize high performance.

4. Introduce more capacitance-controlled electrochemical behavior. At present, most of the reported metal-chalcogenide-based PIB anodes have a limited capacitance-based capacity contribution (<80%), even at high rates. If this part of the capacity contribution can be promoted, the capacity retention at high rates should be enhanced. This would be especially useful for the fast charging required in consumer markets.

5. Devote more efforts into the electrolyte research studies. The suitable coupling of potassium salt and solvent is crucial to forming a stable and efficient SEI film on metal chalcogenides, which is a decisive factor affecting the capacity and cyclability of PIBs. To date, little attention has been paid to the electrolyte.

6. Perform more in situ characterization to understand the underlying potassium storage mechanisms. It is believed that the deeper and clearer understanding of mechanism will help the design of new metal-chalcogenide-based nanostructures, as well as provide inspiration for material modification in the future.

7. Fabricate novel potassium-based hybrid energy storage systems that combine the advantages of different energy storage devices. These new hybrid systems are expected to utilize the superior potassium storage capability of modified metal chalcogenides better, thus obtaining higher energy densities.

It is believed that the challenges facing current metal chalcogenides for PIBs and other potassium-based energy storage systems will be gradually overcome by advances in design, preparation, and characterization techniques, making potassium-based energy storage solutions a practical option for use in daily life.

ORCID
Shilin Zhang https://orcid.org/0000-0002-3268-5708
Tengfei Zhou https://orcid.org/0000-0002-7364-0434

REFERENCES

1. Li M, Lu J, Chen Z, et al. 30 years of lithium-ion batteries. *Adv Mater*. 2018;30(33):1800561.
2. Cheng F, Liang J, Tao Z, et al. Functional materials for rechargeable batteries. *Adv Mater*. 2011;23(15):1695-1715.
3. Kang B, Ceder G. Battery materials for ultrafast charging and discharging. *Nature*. 2009;458(7235):190-193.
4. Zhou J, Qin J, Zhang X, et al. 2D space-confined synthesis of few-layer MoS₂ anchored on carbon nanosheet for lithium-ion battery anode. *ACS Nano*. 2015;9(4):3837-3848.
5. Sun H, Zhang Y, Zhang J, et al. Energy harvesting and storage in 1D devices. *Nat Rev Mater*. 2017;2(6):17023.
6. Zhou L, Zhang K, Hu Z, et al. Recent developments on and prospects for electrode materials with hierarchical structures for lithium-ion batteries. *Adv Energy Mater*. 2018;8(6):1701415.
7. Lu Y, Yu L, Lou XW. Nanostructured conversion-type anode materials for advanced lithium-ion batteries. *Chem*. 2018;4(5):972-996.
8. Zhou J, Qin J, Guo L, et al. Scalable synthesis of high-quality transition metal dichalcogenide nanosheets and their application as sodium-ion battery anodes. *J Mater Chem A*. 2016;4(44):17370-17380.
9. Xue Y, Zhang Q, Wang W, et al. Opening two-dimensional materials for energy conversion and storage: a concept. *Adv Energy Mater*. 2017;7(19):1602684.
10. Zhou J, Li X, Yang C, et al. A quasi-solid-state flexible fiber-shaped Li-CO₂ battery with low overpotential and high energy efficiency. *Adv Mater*. 2018;30:1804439.
11. Li Y, Zhou J, Zhang T, et al. Highly surface-wrinkled and N-doped CNTs anchored on metal wire: a novel fiber-shaped cathode toward high-performance flexible Li-CO₂ batteries. *Adv Funct Mater*. 2019;29:1808117.
12. Zhou J, Qin J, Zhao N, et al. Salt-template-assisted synthesis of robust 3D honeycomb-like structured MoS₂ and its application as a lithium-ion battery anode. *J Mater Chem A*. 2016;4(22):8734-8741.
13. Zhang W, Liu Y, Guo Z. Approaching high-performance potassium-ion batteries via advanced design strategies and engineering. *Sci Adv*. 2019;5(5):eaav7412.
14. Wu X, Chen Y, Xing Z, et al. Advanced carbon-based anodes for potassium-ion batteries. *Adv Energy Mater*. 2019;9(21):1900343.
15. Wu Y, Huang HB, Feng Y, et al. The promise and challenge of phosphorus-based composites as anode materials for potassium-ion batteries. *Adv Mater*. 2019;31:1901414.
16. Yao S, Cui J, Huang J, et al. Rational assembly of hollow microporous carbon spheres as P hosts for long-life sodium-ion batteries. *Adv Energy Mater*. 2018;8(7):1702267.
17. Xu Y, Zhang C, Zhou M, et al. Highly nitrogen doped carbon nanofibers with superior rate capability and cyclability for potassium ion batteries. *Nat Commun*. 2018;9(1):1720.

18. Choi SH, Ko YN, Lee J-K, et al. 3D MoS$_2$-graphene microspheres consisting of multiple nanospheres with superior sodium ion storage properties. *Adv Funct Mater*. 2015;25(12):1780-1788.

19. Yang J, Zhou X, Wu D, et al. S-doped N-rich carbon nanosheets with expanded interlayer distance as anode materials for sodium-ion batteries. *Adv Mater*. 2017;29(6):1604108.

20. Yu Q, Jiang B, Hu J, et al. Metallic octahedral CoSe$_2$ threaded by N-doped carbon nanotubes: a flexible framework for high-performance potassium-ion batteries. *Adv Sci*. 2018;5(10):1800782.

21. Wang T, Zhao N, Shi C, et al. Interface and doping effects on Li ion storage behavior of graphene/Li$_2$O. *J Phys Chem C*. 2017;121(36):19559-19567.

22. Zhang Q, Tan S, Mendes RG, et al. Extremely weak van der Waals coupling in vertical ReS$_2$ nanowalls for high-current-density lithium-ion batteries. *Adv Mater*. 2016;28(13):2616-2623.

23. Ni J, Fu S, Yuan Y, et al. Boosting sodium storage in TiO$_2$ nanotube arrays through surface phosphorylation. *Adv Mater*. 2018;30(6):1704337.

24. Zhu YH, Yuan S, Bao D, et al. Decorating waste cloth via industrial wastewater for tube-type flexible and wearable sodium-ion batteries. *Adv Mater*. 2017;29(16):1603719.

25. Yang J, Ju Z, Jiang Y, et al. Enhanced capacity and rate capability of nitrogen/oxygen dual-doped hard carbon in capacitive potassium-ion storage. *Adv Mater*. 2018;30(4):1700104.

26. Zhang Y, Zhao Y, Ren J, et al. Advances in wearable fiber-shaped lithium-ion batteries. *Adv Mater*. 2016;28(22):4524-4531.

27. Xu Y, Dong H, Zhou M, et al. Ammonium vanadium bronze as a potassium-ion battery cathode with high rate capability and cyclability. *Small Methods*. 2019;3(8):1800349.

28. Qian Y, Jiang S, Li Y, et al. In situ revealing the electroactivity of P-O and P-C bonds in hard carbon for high-capacity and long-life Li/K-ion batteries. *Adv Energy Mater*. 2019;9(34):1901676.

29. Qiu D, Guan J, Li M, et al. Kinetics enhanced nitrogen-doped hierarchical porous hollow carbon spheres boosting advanced potassium-ion hybrid capacitors. *Adv Funct Mater*. 2019;29(32):1903496.

30. Li Z, Dong Y, Feng J, et al. Controllably enriched oxygen vacancies through polymer assistance in titanium pyrophosphate as a super anode for Na/K-ion batteries. *ACS Nano*. 2019;13(8):9227-9236.

31. Zhou X, Chen L, Zhang W, et al. Three-dimensional ordered macroporous metal-organic framework single crystal-derived nitrogen-doped hierarchical porous carbon for high-performance potassium-ion batteries. *Nano Lett*. 2019;19(8):4965-4973.

32. Zhang W, Jiang X, Wang X, et al. Spontaneous weaving of graphitic carbon networks synthesized by pyrolysis of ZIF-67 crystals. *Angew Chem Int Ed*. 2017;56(29):8435-8440.

33. Liu S, Yang B, Zhou J, et al. Nitrogen-rich carbon-onion-constructed nanosheets: an ultrafast and ultrastable dual anode material for sodium and potassium storage. *J Mater Chem A*. 2019;7(31):18499-18509.

34. Ruan J, Wu X, Wang Y, et al. Nitrogen-doped hollow carbon nanosphere towards application of potassium ion storage. *J Mater Chem A*. 2019;7(33):19305-19315.

35. Qiu W, Xiao H, Li Y, et al. Nitrogen and phosphorus codoped vertical graphene/carbon cloth as a binder-free anode for flexible advanced potassium ion full batteries. *Small*. 2019;15(23):1901285.

36. Li Y, Zhong W, Yang C, et al. N/S codoped carbon microboxes with expanded interlayer distance toward excellent potassium storage. *Chem Eng J*. 2019;358:1147-1154.

37. Lu G, Wang H, Zheng Y, et al. Metal-organic framework derived N-doped CNT@ porous carbon for high-performance sodium- and potassium-ion storage. *Electrochim Acta*. 2019;319:541-551.

38. Liu Y, Dai H, Wu L, et al. A large scalable and low-cost sulfur/nitrogen dual-doped hard carbon as the negative electrode material for high-performance potassium-ion batteries. *Adv Energy Mater*. 2019;9(34):1901379.

39. Wang Y, Wang Z, Chen Y, et al. Hyperporous sponge interconnected by hierarchical carbon nanotubes as a high-performance potassium-ion battery anode. *Adv Mater*. 2018;30(32):1802074.

40. Cao B, Zhang Q, Liu H, et al. Graphitic carbon nanocage as a stable and high power anode for potassium-ion batteries. *Adv Energy Mater*. 2018;8(25):1801149.

41. Zhang Z, Jia B, Liu L, et al. Hollow multihole carbon bowls: a stress-release structure design for high-stability and high-volumetric-capacity potassium-ion batteries. *ACS Nano*. 2019;13(10):11363-11371.

42. Zhang W, Ming J, Zhao W, et al. Graphitic nanocarbon with engineered defects for high-performance potassium-ion battery anodes. *Adv Funct Mater*. 2019;29(35):1903641.

43. Li D, Ren X, Ai Q, et al. Facile fabrication of nitrogen-doped porous carbon as superior anode material for potassium-ion batteries. *Adv Energy Mater*. 2018;8(34):1802386.

44. Sun Q, Li D, Cheng J, et al. Nitrogen-doped carbon derived from pre-oxidized pitch for surface dominated potassium-ion storage. *Carbon*. 2019;155:601-610.

45. Liu Q, Fan L, Ma R, et al. Super long-life potassium-ion batteries based on antimony@carbon composite anode. *Chem Commun*. 2018;54(83):11773-11776.

46. Ko YN, Choi SH, Kim H, et al. One-pot formation of Sb-carbon microspheres with graphene sheets: potassium-ion storage properties and discharge mechanisms. *ACS Appl Mater Interfaces*. 2019;11(31):27973-27981.

47. Yang H, Xu R, Yao Y, et al. Multicore-shell bi@N-doped carbon nanospheres for high power density and long cycle life sodium- and potassium-ion anodes. *Adv Funct Mater*. 2019;29(13):1809195.

48. Zhou X, Ge X, Liu S, et al. Enabling superior electrochemical properties for highly efficient potassium storage via impregnating ultrafine Sb nanocrystals within nanochannel-containing carbon nanofibers. *Angew Chem Int Ed*. 2019;131(41):14720-14725.

49. Tong Z, Yang R, Wu S, et al. Surface-engineered black niobium oxide@graphene nanosheets for high-performance sodium−/potassium-ion full batteries. *Small*. 2019;15(28):1901272.

50. Suo G, Li D, Feng L, et al. SnO$_2$ nanosheets grown on stainless steel mesh as a binder free anode for potassium ion batteries. *J Electroanal Chem*. 2019;833:113-118.

51. Wang J, Wang B, Liu Z, et al. Nature of bimetallic oxide Sb$_2$MoO$_6$/rGO anode for high-performance potassium-ion batteries. *Adv Sci*. 2019;6(17):1900904.

52. Tan Q, Li P, Han K, et al. Chemically bubbled hollow Fe$_x$O nanospheres anchored on 3D N-doped few-layer graphene architecture as a performance-enhanced anode material for potassium-ion batteries. *J Mater Chem A*. 2019;7(2):744-754.

53. Chong S, Sun L, Shu C, et al. Chemical bonding boosts nano-rose-like MoS$_2$ anchored on reduced graphene oxide for superior potassium-ion storage. *Nano Energy*. 2019;63:103868.

54. Wang W, Li P, Zheng H, et al. Ultrathin layered SnSe nanoplates for low voltage, high-rate, and long-life alkali-ion batteries. *Small*. 2017;13(46):1702228.

55. Liu Y, Tai Z, Zhang J, et al. Boosting potassium-ion batteries by few-layered composite anodes prepared via solution-triggered one-step shear exfoliation. *Nat Commun*. 2018;9(1): 3645.

56. Chu J, Wang WA, Feng J, et al. Deeply nesting zinc sulfide dendrites in tertiary hierarchical structure for potassium ion batteries: enhanced conductivity from interior to exterior. *ACS Nano*. 2019;13(6):6906-6916.

57. Li D, Sun Q, Zhang Y, et al. Surface-confined SnS$_2$@C@rGO as high-performance anode materials for sodium- and potassium-ion batteries. *ChemSusChem*. 2019;12(12):2689-2700.

58. Yang F, Gao H, Hao J, et al. Yolk-shell structured FeP@C nanoboxes as advanced anode materials for rechargeable lithium−/potassium-ion batteries. *Adv Funct Mater*. 2019;29(16): 1808291.

59. Chen X, Zeng S, Muheiyati H, et al. Double-shelled Ni−Fe−P/N-doped carbon nanobox derived from a prussian blue analogue as an electrode material for K-ion batteries and Li–S batteries. *ACS Energy Lett*. 2019;4(7):1496-1504.

60. Zhang W, Wu Z, Zhang J, et al. Unraveling the effect of salt chemistry on long-durability high-phosphorus-concentration anode for potassium ion batteries. *Nano Energy*. 2018;53:967-974.

61. Bai J, Xi B, Mao H, et al. One-step construction of N,P-codoped porous carbon sheets/CoP hybrids with enhanced lithium and potassium storage. *Adv Mater*. 2018;30(35): 1802310.

62. Zhang W, Pang WK, Sencadas V, et al. Understanding high-energy-density Sn$_4$P$_3$ anodes for potassium-ion batteries. *Joule*. 2018;2(8):1534-1547.

63. Li D, Zhang Y, Sun Q, et al. Hierarchically porous carbon supported Sn$_4$P$_3$ as a superior anode material for potassium-ion batteries. *Energy Storage Mater*. 2019;23:367-374.

64. Liu Z, Li P, Suo G, et al. Zero-strain K$_{0.6}$Mn$_1$F$_{2.7}$ hollow nanocubes for ultrastable potassium ion storage. *Energ Environ Sci*. 2018;11(10):3033-3042.

65. Lu M, Wang KF, Ke HD, et al. Potassium vanadate K$_2$V$_3$O$_8$ as a superior anode material for potassium-ion batteries. *Mater Lett*. 2018;232:224-227.

66. Cao K, Liu H, Li W, et al. K$_2$Ti$_6$O$_{13}$ nanorods for potassium-ion battery anodes. *J Electroanal Chem*. 2019;841:51-55.

67. Peng B, Li Y, Gao J, et al. High energy K-ion batteries based on P3-type K$_{0.5}$MnO$_2$ hollow submicrosphere cathode. *J Power Sources*. 2019;437:226913.

68. Zhao S, Yan K, Munroe P, et al. Construction of hierarchical K$_{1.39}$Mn$_3$O$_6$ spheres via AlF$_3$ coating for high-performance potassium-ion batteries. *Adv Energy Mater*. 2019;9(10):1803757.

69. Tan H, Du X, Huang J, et al. KVPO$_4$F as a novel insertion-type anode for potassium ion batteries. *Chem Commun*. 2019; 55(75):11311-11314.

70. Wei Z, Wang D, Li M, et al. Fabrication of hierarchical potassium titanium phosphate spheroids: a host material for sodium-ion and potassium-ion storage. *Adv Energy Mater*. 2018;8(27):1801102.

71. Deng L, Yang Z, Tan L, et al. Investigation of the Prussian blue analog Co$_3$[Co(CN)$_6$]$_2$ as an anode material for non-aqueous potassium-ion batteries. *Adv Mater*. 2018;30(31): 1802510.

72. Chong S, Wu Y, Guo S, et al. Potassium nickel hexacyanoferrate as cathode for high voltage and ultralong life potassium-ion batteries. *Energy Storage Mater*. 2019;22: 120-127.

73. Chen X, Zhang H, Ci C, et al. Few-layered boronic ester based covalent organic frameworks/carbon nanotube composites for high-performance K-organic batteries. *ACS Nano*. 2019;13(3): 3600-3607.

74. Zhang H, Sun W, Chen X, et al. Few-layered fluorinated triazine-based covalent organic Nanosheets for high-performance alkali organic batteries. *ACS Nano*. 2019;13(12): 14252-14261.

75. Liang Y, Luo C, Wang F, et al. An organic anode for high temperature potassium-ion batteries. *Adv Energy Mater*. 2019;9(2): 1802986.

76. Wang C, Tang W, Yao Z, et al. Potassium perylene-tetracarboxylate with two-electron redox behaviors as a highly stable organic anode for K-ion batteries. *Chem Commun*. 2019;55(12):1801-1804.

77. Bai Y, Fu W, Chen W, et al. Perylenetetracarboxylic diimide as a high-rate anode for potassium-ion batteries. *J Mater Chem A*. 2019;7(42):24454-24461.

78. Zhu Y, Chen P, Zhou Y, et al. New family of organic anode without aromatics for energy storage. *Electrochim Acta*. 2019; 318:262-271.

79. Zhang C, Qiao Y, Xiong P, et al. Conjugated microporous polymers with tunable electronic structure for high-performance potassium-ion batteries. *ACS Nano*. 2019;13(1): 745-754.

80. Chen C, Yang Y, Tang X, et al. Graphene-encapsulated FeS$_2$ in carbon fibers as high reversible anodes for Na$^+$/K$^+$ batteries in a wide temperature range. *Small*. 2019;15(10):1804740.

81. Li L, Zhang W, Wang X, et al. Hollow-carbon-templated few-layered V$_5$S$_8$ nanosheets enabling ultrafast potassium storage and long-term cycling. *ACS Nano*. 2019;13(7):7939-7948.

82. Vasileff A, Zheng Y, Qiao SZ. Carbon solving carbon's problems: recent progress of nanostructured carbon-based catalysts for the electrochemical reduction of CO$_2$. *Adv Energy Mater*. 2017;7(21):1700759.

83. Sun C, Dong Q, Yang J, et al. Metal-organic framework derived CoSe$_2$ nanoparticles anchored on carbon fibers as bifunctional electrocatalysts for efficient overall water splitting. *Nano Res*. 2016;9(8):2234-2243.

84. Yang L, Zhou W, Lu J, et al. Hierarchical spheres constructed by defect-rich MoS$_2$/carbon nanosheets for efficient electrocatalytic hydrogen evolution. *Nano Energy*. 2016;22: 490-498.

85. Han X, Zhang W, Ma X, et al. Identifying the activation of bimetallic sites in NiCo$_2$S$_4$@g-C$_3$N$_4$-CNT hybrid electrocatalysts for synergistic oxygen reduction and evolution. *Adv Mater*. 2019;31(18):1808281.

86. Qiao Y, Yuan P, Hu Y, et al. Sulfuration of an Fe-N-C catalyst containing Fe_xC/Fe species to enhance the catalysis of oxygen reduction in acidic media and for use in flexible Zn-air batteries. *Adv Mater*. 2018;30(46):1804504.

87. Deng Z, Jiang H, Hu Y, et al. 3D ordered macroporous MoS_2@C nanostructure for flexible Li-ion batteries. *Adv Mater*. 2017;29(10):1603020.

88. Wang J, Liu J, Chao D, et al. Self-assembly of honeycomb-like MoS_2 nanoarchitectures anchored into graphene foam for enhanced lithium-ion storage. *Adv Mater*. 2014;26(42):7162-7169.

89. Yu H, Cheng X, Xia M, et al. Pretreated commercial $TiSe_2$ as an insertion-type potassium container for constructing "rocking-chair" type potassium ion batteries. *Energy Storage Mater*. 2019;22:154-159.

90. Jia B, Yu Q, Zhao Y, et al. Bamboo-like hollow tubes with MoS_2/N-doped-C interfaces boost potassium-ion storage. *Adv Funct Mater*. 2018;28(40):1803409.

91. Tian H, Yu X, Shao H, et al. Unlocking few-layered ternary chalcogenides for high-performance potassium-ion storage. *Adv Energy Mater*. 2019;9(29):1901560.

92. Zhao Y, Zhu J, Ong SJH, et al. High-rate and ultralong cycle-life potassium ion batteries enabled by in situ engineering of yolk-shell FeS_2@C structure on graphene matrix. *Adv Energy Mater*. 2018;8(36):1802565.

93. Fang L, Xu J, Sun S, et al. Few-layered tin sulfide nanosheets supported on reduced graphene oxide as a high-performance anode for potassium-ion batteries. *Small*. 2019;15(10):1804806.

94. Miao W, Zhang Y, Li H, et al. ZIF-8/ZIF-67-derived 3D amorphous carbon-encapsulated CoS/NCNTs supported on CoS-coated carbon nanofibers as an advanced potassium-ion battery anode. *J Mater Chem A*. 2019;7(10):5504-5512.

95. Xu L, Xiong P, Zeng L, et al. Electrospun $VSe_{1.5}$/CNF composite with excellent performance for alkali metal ion batteries. *Nanoscale*. 2019;11(35):16308-16316.

96. Ge J, Fan L, Wang J, et al. $MoSe_2$/N-doped carbon as anodes for potassium-ion batteries. *Adv Energy Mater*. 2018;8(29):1801477.

97. Wu Z, Liang G, Pang WK, et al. Coupling topological insulator $SnSb_2Te_4$ nanodots with highly doped graphene for high-rate energy storage. *Adv Mater*. 2020;32(2):1905632.

98. Yi Y, Sun Z, Li C, et al. Designing 3D biomorphic nitrogen-doped $MoSe_2$/graphene composites toward high-performance potassium-ion capacitors. *Adv Funct Mater*. 2019;29:1903878.

99. Liu Y, Tai Z, Zhang Q, et al. A new energy storage system: rechargeable potassium-selenium battery. *Nano Energy*. 2017;35:36-43.

100. Xiong P, Han X, Zhao X, et al. Room-temperature potassium-sulfur batteries enabled by microporous carbon stabilized small-molecule sulfur cathodes. *ACS Nano*. 2019;13(2):2536-2543.

101. Xiao N, Gourdin G, Wu Y. Simultaneous stabilization of potassium metal and superoxide in $K-O_2$ batteries on the basis of electrolyte reactivity. *Angew Chem Int Ed*. 2018;57(34):10864-10867.

102. Gao H, Zhou T, Zheng Y, et al. CoS quantum dot nanoclusters for high-energy potassium-ion batteries. *Adv Funct Mater*. 2017;27(43):1702634.

103. Zhou J, Wang L, Yang M, et al. Hierarchical VS_2 nanosheet assemblies: a universal host material for the reversible storage of alkali metal ions. *Adv Mater*. 2017;29(35):1702061.

104. He C, Zhang JH, Zhang WX, et al. GeSe/BP van der Waals heterostructures as promising anode materials for potassium-ion batteries. *J Phys Chem C*. 2019;123(9):5157-5163.

105. Yi Z, Qian Y, Tian J, et al. Self-templating growth of Sb_2Se_3@C microtube: a convention-alloying-type anode material for enhanced K-ion batteries. *J Mater Chem A*. 2019;7(19):12283-12291.

106. Wang L, Zou J, Chen S, et al. TiS_2 as a high performance potassium ion battery cathode in ether-based electrolyte. *Energy Storage Mater*. 2018;12:216-222.

107. Tian B, Tang W, Leng K, et al. Phase transformations in TiS_2 during K intercalation. *ACS Energy Lett*. 2017;2(8):1835-1840.

108. Zhang R, Bao J, Pan Y, et al. Highly reversible potassium-ion intercalation in tungsten disulfide. *Chem Sci*. 2019;10(9):2604-2612.

109. Zhao D, Zhang L, Fu C, et al. The lithium and sodium storage performances of phosphorus and its hierarchical structure. *Nano Res*. 2018;12(1):1-17.

110. Zhou J, Zhao H, Zhang Q, et al. Carbon nanotube-stabilized Co_9S_8 dual-shell hollow spheres for high-performance K-ion storage. *Chem Commun*. 2019;55(10):1406-1409.

111. Yao Q, Zhang J, Li J, et al. Yolk-shell NiS_x@C nanosheets as K-ion battery anode with high rate capability and ultralong cycle life. *J Mater Chem A*. 2019;7(32):18932-18939.

112. He H, Huang D, Gan Q, et al. Anion vacancies regulating endows MoSSe with fast and stable potassium ion storage. *ACS Nano*. 2019;13:11843-11852.

113. Mao M, Cui C, Wu M, et al. Flexible ReS_2 nanosheets/N-doped carbon nanofibers-based paper as a universal anode for alkali (Li, Na, K) ion battery. *Nano Energy*. 2018;45:346-352.

114. Liao Y, Chen C, Yin D, et al. Improved Na^+/K^+ storage properties of $ReSe_2$-carbon nanofibers based on graphene modifications. *Nano-Micro Lett*. 2019;11(1):22.

115. Wang J, Fan L, Liu Z, et al. In situ alloying strategy for exceptional potassium ion batteries. *ACS Nano*. 2019;13(3):3703-3713.

116. Zhang M, Shoaib M, Fei H, et al. Hierarchically porous N-doped carbon fibers as a free-standing anode for high-capacity potassium-based dual-ion battery. *Adv Energy Mater*. 2019;9(37):1901663.

117. Zhang Q, Wang Z, Zhang S, et al. Cathode materials for potassium-ion batteries: current status and perspective. *Electrochem Energy Rev*. 2018;1(4):625-658.

118. Li L, Zheng Y, Zhang S, et al. Recent progress on sodium ion batteries: potential high-performance anodes. *Energ Environ Sci*. 2018;11(9):2310-2340.

119. Zheng Y, Zhou T, Zhao X, et al. Atomic interface engineering and electric-field effect in ultrathin Bi_2MoO_6 nanosheets for superior lithium ion storage. *Adv Mater*. 2017;29(26):1700396.

120. Cuan J, Zhou Y, Zhou T, et al. Borohydride-scaffolded Li/Na/mg fast ionic conductors for promising solid-state electrolytes. *Adv Mater*. 2019;31(1):1803533.

121. Zhang S, Zheng Y, Huang X, et al. Structural engineering of hierarchical micro-nanostructured Ge-C framework by controlling the nucleation for ultralong-life Li storage. *Adv Energy Mater*. 2019;9(19):1900081.

122. Dai L, Zhang W, Hu C, et al. High-performance K-CO$_2$ batteries based on metal-free bifunctional carbon electrocatalysts. *Angew Chem Int Ed*. 2020;59:3470-3474. https://doi.org/10.1002/anie.201913687.

123. Cuan J, Zhang F, Zheng Y, et al. Heterocarbides reinforced electrochemical energy storage. *Small*. 2019;15(44):1903652.

124. Mao J, Zhou T, Zheng Y, et al. Two-dimensional nanostructures for sodium-ion battery anodes. *J Mater Chem A*. 2018;6(8):3284-3303.

125. Tai Z, Liu Y, Zhang Q, et al. Ultra-light and flexible pencil-trace anode for high performance potassium-ion and lithium-ion batteries. *Green Energy Environ*. 2017;2(3):278-284.

126. Ren X, Zhao Q, McCulloch WD, et al. MoS$_2$ as a long-life host material for potassium ion intercalation. *Nano Res*. 2017;10(4):1313-1321.

127. Cao X, Tan C, Sindoro M, et al. Hybrid micro−/nano-structures derived from metal-organic frameworks: preparation and applications in energy storage and conversion. *Chem Soc Rev*. 2017;46(10):2660-2677.

128. Hwang JY, Kim HM, Yoon CS, et al. Toward high-safety potassium-sulfur batteries using a potassium polysulfide catholyte and metal-free anode. *ACS Energy Lett*. 2018;3(3):540-541.

129. Yao Y, Xu R, Chen M, et al. Encapsulation of SeS$_2$ into nitrogen-doped free-standing carbon nanofiber film enabling long cycle life and high energy density K-SeS$_2$ battery. *ACS Nano*. 2019;13(4):4695-4704.

130. Ren X, Wu Y. A low-overpotential potassium-oxygen battery based on potassium superoxide. *J Am Chem Soc*. 2013;135(8):2923-2926.

131. Hwang JY, Kim HM, Sun YK. High performance potassium-sulfur batteries based on a sulfurized polyacrylonitrile cathode and polyacrylic acid binder. *J Mater Chem A*. 2018;6(30):14587-14593.

132. Zhao Q, Hu Y, Zhang K, et al. Potassium-sulfur batteries: a new member of room-temperature rechargeable metal-sulfur batteries. *Inorg Chem*. 2014;53(17):9000-9005.

133. Chen T, Zhang Z, Cheng B, et al. Self-templated formation of interlaced carbon nanotubes threaded hollow Co$_3$S$_4$ nanoboxes for high-rate and heat-resistant lithium-sulfur batteries. *J Am Chem Soc*. 2017;139(36):12710-12715.

134. Chen T, Ma L, Cheng B, et al. Metallic and polar Co$_9$S$_8$ inlaid carbon hollow nanopolyhedra as efficient polysulfide mediator for lithium-sulfur batteries. *Nano Energy*. 2017;38:239-248.

135. Yang T, Guo B, Du W, et al. Design and construction of sodium polysulfides defense system for room-temperature Na-S battery. *Adv Sci*. 2019;6(23):1901557.

136. Yan Z, Xiao J, Lai W, et al. Nickel sulfide nanocrystals on nitrogen-doped porous carbon nanotubes with high-efficiency electrocatalysis for room-temperature sodium-sulfur batteries. *Nat Commun*. 2019;10(1):4793.

137. Zhang K, Chen H, Wang X, et al. Synthesis and structure determination of potassium copper selenide nanowires and solid-state supercapacitor application. *J Power Sources*. 2014;268:522-532.

138. Kravchyk KV, Bhauriyal P, Piveteau L, et al. High-energy-density dual-ion battery for stationary storage of electricity using concentrated potassium fluorosulfonylimide. *Nat Commun*. 2018;9(1):4469.

139. Ji B, Zhang F, Song X, et al. A novel potassium-ion-based dual-ion battery. *Adv Mater*. 2017;29(19):1700519.

140. Bellani S, Wang F, Longoni G, et al. WS$_2$-graphite dual-ion batteries. *Nano Lett*. 2018;18(11):7155-7164.

141. Wang S, Tu J, Xiao J, et al. 3D skeleton nanostructured Ni$_3$S$_2$/Ni foam@RGO composite anode for high-performance dual-ion battery. *J Energy Chem*. 2019;28:144-150.

142. Li Z, Yang L, Xu G, et al. Hierarchical MoS$_2$@N-doped carbon hollow spheres with enhanced performance in sodium dual-ion batteries. *ChemElectroChem*. 2018;6(3):661-667.

143. Zhu H, Zhang F, Li J, et al. Penne-like MoS$_2$/carbon nanocomposite as anode for sodium-ion-based dual-ion battery. *Small*. 2018;14(13):1703951.

144. Liu Y, Hu X, Zhong G, et al. Layer-by-layer stacked nanohybrids of N,S-co-doped carbon film modified atomic MoS$_2$ nanosheets for advanced sodium dual-ion batteries. *J Mater Chem A*. 2019;7(42):24271-24280.

145. Wang P, Li C, Dong S, et al. Hierarchical NiCo$_2$S$_4$@NiO core–shell heterostructures as catalytic cathode for long-life Li-O$_2$ batteries. *Adv Energy Mater*. 2019;9(24):1900788.

146. Ju B, Song HJ, Lee GH, et al. Nickel disulfide nanosheet as promising cathode electrocatalyst for long-life lithium–oxygen batteries. *Energy Storage Mater*. 2020;24:594-601.

147. Hou Z, Feng S, Hei P, et al. Morphology regulation of Li$_2$O$_2$ by flower-like ZnCo$_2$S$_4$ enabling high performance Li-O$_2$ battery. *J Power Sources*. 2019;441:227168.

148. Hu A, Long J, Shu C, et al. Three-dimensional CoNi$_2$S$_4$ nanorod arrays anchored on carbon textiles as an integrated cathode for high-rate and long-life lithium-oxygen battery. *Electrochim Acta*. 2019;301:69-79.

149. Long J, Hou Z, Shu C, et al. Free-standing three-dimensional CuCo$_2$S$_4$ nanosheet array with high catalytic activity as an efficient oxygen electrode for lithium-oxygen batteries. *ACS Appl Mater Interfaces*. 2019;11(4):3834-3842.

150. Tan P, Chen B, Xu H, et al. Flexible Zn- and Li-air batteries: recent advances, challenges, and future perspectives. *Energ Environ Sci*. 2017;10(10):2056-2080.

151. Feng N, He P, Zhou H. Critical challenges in rechargeable aprotic Li-O$_2$ batteries. *Adv Energy Mater*. 2016;6(9):1502303.

152. Hartmann P, Bender CL, Vracar M, et al. A rechargeable room-temperature sodium superoxide (NaO$_2$) battery. *Nat Mater*. 2013;12(3):228-232.

AUTHOR BIOGRAPHIES

JINGWEN ZHOU is working as a research assistant in Institute of Chemical Materials, China Academy of Engineering Physics. He received his BS degree and MS degree from Tianjin University in 2014 and 2017, respectively. He is now going to purse his PhD degree in the University of Wollongong from 2020. His research direction focuses on design and synthesis of multidimensional nanocomposites and their applications on novel flexible energy storage systems like metal-gas batteries and alkali metal-ion batteries.
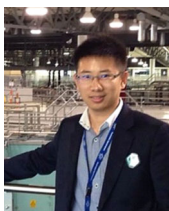
TENGFEI ZHOU is currently an Australian Research Council DECRA fellow at the University of Wollongong (UOW), Australia. He received his PhD degree from the University of Wollongong in 2016. His research focuses on charge transfer processes in new-generation energy storage and conversion, such as metal-ion batteries and photocatalysis.

ZAIPING GUO is now working at Institute of Superconducting and Electronic Materials, University of Wollongong (Australia). She received her PhD degree from University of Wollongong in 2003, and her BSc and MSc degrees in 1993 and 1996 from Xinjiang University (China), respectively. Her current research interests mainly focused on the energy storage such as lithium ion batteries, sodium ion batteries, potassium ion batteries, and hydrogen storage, as well as electrochemistry characterization and computer modeling.